EUROPEAN ORGANIZATION FOR NUCLEAR RESEARCH (CERN)

CERN-EP/2003-084
December 2, 2003

Studies of QCD at e^+e^- Centre-of-Mass Energies between 91 and 209 GeV

The ALEPH Collaboration *)

Abstract

The hadronic final states observed with the ALEPH detector at LEP in e^+e^- annihilation are analysed using 730 pb^{-1} of data collected between 91 and 209 GeV in the framework of QCD. In particular event-shape variables and inclusive charged particle spectra are measured. The energy evolution of quantities derived from these measurements is compared to analytic QCD predictions. The mean charged particle multiplicity, the charged particle momentum spectrum and its peak position are compared to predictions of the modified-leading-logarithmic approximation. The strong coupling constant α_s is determined from a fit of the QCD prediction to distributions of six event-shape variables at eight centre-of-mass energies. A study of non-perturbative power law corrections is presented.

submitted to The European Physical Journal C

---

*) See next pages for the list of authors

The ALEPH Collaboration

A. Heister, S. Schael

Physikalisches Institut das RWTH-Aachen, D-52056 Aachen, Germany

R. Barate, R. Brunelière, I. De Bonis, D. Decamp, C. Goy, S. Jézéquel, J.-P. Lees, F. Martin, E. Merle, M.-N. Minard, B. Pietrzyk, B. Trocmé

Laboratoire de Physique des Particules (LAPP), IN^{2}P^3-CNRS, F-74019 Annecy-le-Vieux Cedex, France

S. Bravo, M.P. Casado, M. Chmeissani, J.M. Crespo, E. Fernandez, M. Fernandez-Bosman, Ll. Garrido,[15] M. Martinez, A. Pacheco, H. Ruiz

Institut de Física d'Altes Energies, Universitat Autònoma de Barcelona, E-08193 Bellaterra (Barcelona), Spain[7]

A. Colaleo, D. Creanza, N. De Filippis, M. de Palma, G. Iaselli, G. Maggi, M. Maggi, S. Nuzzo, A. Ranieri, G. Raso,[24] F. Ruggieri, G. Selvaggi, L. Silvestris, P. Tempesta, A. Tricomi,[3] G. Zito

Dipartimento di Fisica, INFN Sezione di Bari, I-70126 Bari, Italy

X. Huang, J. Lin, Q. Ouyang, T. Wang, Y. Xie, R. Xu, S. Xue, J. Zhang, L. Zhang, W. Zhao

Institute of High Energy Physics, Academia Sinica, Beijing, The People's Republic of China[8]

D. Abbaneo, T. Barklow,[26] O. Buchmüller,[26] M. Cattaneo, B. Clerbaux,[23] H. Drevermann, R.W. Forty, M. Frank, F. Gianotti, J.B. Hansen, J. Harvey, D.E. Hutchcroft,[30], P. Janot, B. Jost, M. Kado,[2] P. Mato, A. Moutoussi, F. Ranjard, L. Rolandi, D. Schlatter, G. Sguazzoni, F. Teubert, A. Valassi, I. Videau

European Laboratory for Particle Physics (CERN), CH-1211 Geneva 23, Switzerland

F. Badaud, S. Dessagne, A. Falvard,[20] D. Fayolle, P. Gay, J. Jousset, B. Michel, S. Monteil, D. Pallin, J.M. Pascolo, P. Perret

Laboratoire de Physique Corpusculaire, Université Blaise Pascal, IN^{2}P^3-CNRS, Clermont-Ferrand, F-63177 Aubière, France

J.D. Hansen, J.R. Hansen, P.H. Hansen, A.C. Kraan, B.S. Nilsson

Niels Bohr Institute, 2100 Copenhagen, DK-Denmark[9]

A. Kyriakis, C. Markou, E. Simopoulou, A. Vayaki, K. Zachariadou

Nuclear Research Center Demokritos (NRCD), GR-15310 Attiki, Greece

A. Blondel,[12] J.-C. Brient, F. Machefert, A. Rougé, H. Videau

Laoratoire Leprince-Ringuet, Ecole Polytechnique, IN^{2}P^3-CNRS, F-91128 Palaiseau Cedex, France

V. Ciulli, E. Focardi, G. Parrini

Dipartimento di Fisica, Università di Firenze, INFN Sezione di Firenze, I-50125 Firenze, Italy

A. Antonelli, M. Antonelli, G. Bencivenni, F. Bossi, G. Capon, F. Cerutti, V. Chiarella, P. Laurelli, G. Mannocchi,[5] G.P. Murtas, L. Passalacqua

Laboratori Nazionali dell'INFN (LNF-INFN), I-00044 Frascati, Italy

J. Kennedy, J.G. Lynch, P. Negus, V. O'Shea, A.S. Thompson

Department of Physics and Astronomy, University of Glasgow, Glasgow G12 8QQ,United Kingdom[10]

S. Wasserbaech

Utah Valley State College, Orem, UT 84058, U.S.A.

R. Cavanaugh,[4] S. Dhamotharan,[21] C. Geweniger, P. Hanke, V. Hepp, E.E. Kluge, A. Putzer, H. Stenzel, K. Tittel, M. Wunsch[19]

Kirchhoff-Institut für Physik, Universität Heidelberg, D-69120 Heidelberg, Germany[16]

R. Beuselinck, W. Cameron, G. Davies, P.J. Dornan, M. Girone,[1] R.D. Hill, N. Marinelli, J. Nowell, S.A. Rutherford, J.K. Sedgbeer, J.C. Thompson,[14] R. White

Department of Physics, Imperial College, London SW7 2BZ, United Kingdom[10]

V.M. Ghete, P. Girtler, E. Kneringer, D. Kuhn, G. Rudolph

Institut für Experimentalphysik, Universität Innsbruck, A-6020 Innsbruck, Austria[18]

E. Bouhova-Thacker, C.K. Bowdery, D.P. Clarke, G. Ellis, A.J. Finch, F. Foster, G. Hughes, R.W.L. Jones, M.R. Pearson, N.A. Robertson, M. Smizanska

Department of Physics, University of Lancaster, Lancaster LA1 4YB, United Kingdom[10]

O. van der Aa, C. Delaere,[28] G.Leibenguth,[31] V. Lemaitre[29]

Institut de Physique Nucléaire, Département de Physique, Université Catholique de Louvain, 1348 Louvain-la-Neuve, Belgium

U. Blumenschein, F. Hölldorfer, K. Jakobs, F. Kayser, K. Kleinknecht, A.-S. Müller, B. Renk, H.-G. Sander, S. Schmeling, H. Wachsmuth, C. Zeitnitz, T. Ziegler

Institut für Physik, Universität Mainz, D-55099 Mainz, Germany[16]

A. Bonissent, P. Coyle, C. Curtil, A. Ealet, D. Fouchez, P. Payre, A. Tilquin

Centre de Physique des Particules de Marseille, Univ Méditerranée, IN^{2}P^3-CNRS, F-13288 Marseille, France

F. Ragusa

Dipartimento di Fisica, Università di Milano e INFN Sezione di Milano, I-20133 Milano, Italy.

A. David, H. Dietl,[32] G. Ganis,[27] K. Hüttmann, G. Lütjens, W. Männer[32], H.-G. Moser, R. Settles, M. Villegas, G. Wolf

Max-Planck-Institut für Physik, Werner-Heisenberg-Institut, D-80805 München, Germany[16]

J. Boucrot, O. Callot, M. Davier, L. Duflot, J.-F. Grivaz, Ph. Heusse, A. Jacholkowska,[6] L. Serin, J.-J. Veillet

Laboratoire de l'Accélérateur Linéaire, Université de Paris-Sud, IN^{2}P^3-CNRS, F-91898 Orsay Cedex, France

P. Azzurri, G. Bagliesi, T. Boccali, L. Foà, A. Giammanco, A. Giassi, F. Ligabue, A. Messineo, F. Palla, G. Sanguinetti, A. Sciabà, P. Spagnolo, R. Tenchini, A. Venturi, P.G. Verdini

Dipartimento di Fisica dell'Università, INFN Sezione di Pisa, e Scuola Normale Superiore, I-56010 Pisa, Italy

O. Awunor, G.A. Blair, G. Cowan, A. Garcia-Bellido, M.G. Green, T. Medcalf, A. Misiejuk, J.A. Strong, P. Teixeira-Dias

Department of Physics, Royal Holloway & Bedford New College, University of London, Egham, Surrey TW20 OEX, United Kingdom[10]

R.W. Clifft, T.R. Edgecock, P.R. Norton, I.R. Tomalin, J.J. Ward

Particle Physics Dept., Rutherford Appleton Laboratory, Chilton, Didcot, Oxon OX11 OQX, United Kingdom[10]

B. Bloch-Devaux, D. Boumediene, P. Colas, B. Fabbro, E. Lançon, M.-C. Lemaire, E. Locci, P. Perez, J. Rander, B. Tuchming, B. Vallage

CEA, DAPNIA/Service de Physique des Particules, CE-Saclay, F-91191 Gif-sur-Yvette Cedex, France[17]

A.M. Litke, G. Taylor

Institute for Particle Physics, University of California at Santa Cruz, Santa Cruz, CA 95064, USA[22]

C.N. Booth, S. Cartwright, F. Combley,[25] P.N. Hodgson, M. Lehto, L.F. Thompson

Department of Physics, University of Sheffield, Sheffield S3 7RH, United Kingdom[10]

A. Böhrer, S. Brandt, C. Grupen, J. Hess, A. Ngac, G. Prange

Fachbereich Physik, Universität Siegen, D-57068 Siegen, Germany[16]

C. Borean, G. Giannini

Dipartimento di Fisica, Università di Trieste e INFN Sezione di Trieste, I-34127 Trieste, Italy

H. He, J. Putz, J. Rothberg

Experimental Elementary Particle Physics, University of Washington, Seattle, WA 98195 U.S.A.

S.R. Armstrong, K. Berkelman, K. Cranmer, D.P.S. Ferguson, Y. Gao,[13] S. González, O.J. Hayes, H. Hu, S. Jin, J. Kile, P.A. McNamara III, J. Nielsen, Y.B. Pan, J.H. von Wimmersperg-Toeller, W. Wiedenmann, J. Wu, Sau Lan Wu, X. Wu, G. Zobernig

Department of Physics, University of Wisconsin, Madison, WI 53706, USA[11]

G. Dissertori

Institute for Particle Physics, ETH Hönggerberg, 8093 Zürich, Switzerland.

[1]Also at CERN, 1211 Geneva 23, Switzerland.
[2]Now at Fermilab, PO Box 500, MS 352, Batavia, IL 60510, USA
[3]Also at Dipartimento di Fisica di Catania and INFN Sezione di Catania, 95129 Catania, Italy.
[4]Now at University of Florida, Department of Physics, Gainesville, Florida 32611-8440, USA
[5]Also IFSI sezione di Torino, CNR, Italy.
[6]Also at Groupe d'Astroparticules de Montpellier, Université de Montpellier II, 34095, Montpellier, France.
[7]Supported by CICYT, Spain.
[8]Supported by the National Science Foundation of China.
[9]Supported by the Danish Natural Science Research Council.
[10]Supported by the UK Particle Physics and Astronomy Research Council.
[11]Supported by the US Department of Energy, grant DE-FG0295-ER40896.
[12]Now at Departement de Physique Corpusculaire, Université de Genève, 1211 Genève 4, Switzerland.
[13]Also at Department of Physics, Tsinghua University, Beijing, The People's Republic of China.
[14]Supported by the Leverhulme Trust.
[15]Permanent address: Universitat de Barcelona, 08208 Barcelona, Spain.
[16]Supported by Bundesministerium für Bildung und Forschung, Germany.
[17]Supported by the Direction des Sciences de la Matière, C.E.A.
[18]Supported by the Austrian Ministry for Science and Transport.
[19]Now at SAP AG, 69185 Walldorf, Germany
[20]Now at Groupe d' Astroparticules de Montpellier, Université de Montpellier II, 34095 Montpellier, France.
[21]Now at BNP Paribas, 60325 Frankfurt am Mainz, Germany
[22]Supported by the US Department of Energy, grant DE-FG03-92ER40689.
[23]Now at Institut Inter-universitaire des hautes Energies (IIHE), CP 230, Université Libre de Bruxelles, 1050 Bruxelles, Belgique
[24]Also at Dipartimento di Fisica e Tecnologie Relative, Università di Palermo, Palermo, Italy.
[25]Deceased.
[26]Now at SLAC, Stanford, CA 94309, U.S.A
[27]Now at IWR, Forschungzentrum Karlsruhe, Postfach 3640, 76021 Karlsruhe, Germany
[28]Research Fellow of the Belgium FNRS
[29]Research Associate of the Belgium FNRS
[30]Now at Liverpool University, Liverpool L69 7ZE, United Kingdom
[31]Supported by the Federal Office for Scientific, Technical and Cultural Affairs through the Interuniversity Attraction Pole P5/27
[32]Now at INP, Cracow, Poland

1 Introduction

A study of the structure of hadronic events registered by the ALEPH detector at LEP at centre-of-mass energies E_{cm} between 91 and 209 GeV is presented. The measurements include event-shape variables, jet rates and inclusive charged particle distributions. The primary objective of these measurements is to compare their energy evolution with the prediction of QCD. The data are analysed in a global manner to ease the study of the systematic uncertainties and their correlation. The data presented in [1] at 91.2 GeV and in [2] at 133 GeV have been re-processed using an improved selection and correction procedure. The higher energy data at average centre-of-mass energies of 161, 172, 183, 189, 200 and 206 GeV are published here for the first time. The numerical results of the numerous measurements performed for this publication are archived on the ALEPH QCD web site [3].

A large part of this paper is devoted to measurements of α_s from event-shape variables. The prescription for the theoretical predictions and the assessment of theoretical uncertainties related to missing higher orders are applied in this analysis, as recommended in [4]. Non-perturbative aspects of the determination of α_s using event-shape variables are studied by means of power laws, which are corrections scaling with powers of $1/Q$ [5], where Q is the four-momentum transfer. At leading order Q is equal to $\sqrt{s}$ (or E_{cm}) in $\mathrm{e^+e^-}$ annihilation so that these quantities are used interchangeably in this article.

This paper is organised as follows. In Section 2, brief descriptions of the ALEPH detector, of the overall event-selection method and of the correction procedure are given. Distributions of inclusive observables are presented in Section 3 and jet rates in Section 4, followed by event-shape variables in Section 5. These measurements are analysed in Section 6 to determine α_s. Systematic uncertainties of the measurements of α_s are given in Section 7. Results using different variables and different energies are combined in Section 8. A study of power law corrections is described in Section 9. Section 10 gives the summary and conclusions. The most relevant theoretical predictions for this paper are compiled in the Appendix.

2 Experimental Procedure

2.1 The ALEPH Detector

The ALEPH detector is described in detail in [6] and its performance in [7]. The central part of the detector is dedicated to the reconstruction of the trajectories of charged particles. The path of these particles is measured by a two-layer silicon strip vertex detector (VDET), a cylindrical drift chamber (ITC) and a large time projection chamber (TPC). The three tracking detectors are immersed in a 1.5 T axial magnetic field provided by a superconducting solenoidal coil. Together they measure charged particle transverse momenta with a resolution of $\delta p_{\mathrm{t}}/p_{\mathrm{t}} = 6 \times 10^{-4} p_{\mathrm{t}} \oplus 0.005$ (p_{t} in GeV/c). In the following, *good tracks* are defined as charged particle tracks reconstructed with at least four hits in the TPC, originating from within a cylinder of length 20 cm and radius 2 cm coaxial with the beam and centred at the nominal collision point.

Electrons and photons are identified in the electromagnetic calorimeter (ECAL), situated between the TPC and the coil. The ECAL is a sampling calorimeter sandwich

of lead plates and proportional wire chambers segmented in $0.9^\circ \times 0.9^\circ$ projective towers and read out in three sections in depth. It has a total thickness of 22 radiation lengths and yields a relative energy resolution of $0.18/\sqrt{E} + 0.009$, with E in GeV, for isolated photons. The iron return yoke, instrumented with 23 layers of streamer tubes, forms the hadron calorimeter (HCAL) and provides a relative energy resolution for charged and neutral hadrons of $0.85/\sqrt{E}$. Muons are distinguished from hadrons by their characteristic pattern in HCAL and by the muon chambers, composed of two double-layers of streamer tubes outside HCAL.

The information from the tracking detectors and the calorimeters is combined in an energy-flow algorithm [7]. For each event, the algorithm provides a set of charged and neutral reconstructed particles, called *energy-flow objects*, with measured momentum vectors and information on particle type. The energy-flow objects used in this analysis are required to have a polar angle θ with respect to the beam such that $|\cos\theta| < 0.95$ and a minimum transverse momentum of 200 MeV/c.

2.2 Event Selection

The selection of hadronic events collected at the Z resonance is described in [1]. Events are accepted with at least five good tracks and with a total charged energy in excess of 15 GeV. Energy-flow objects are used to determine the sphericity axis and its polar angle $\Theta_{\rm sph}$ is required to be such that $|\cos\Theta_{\rm sph}| < 0.9$ to ensure that the event is well contained within the detector.

The same criteria are applied to the selection of $\mathrm{q\overline{q}}(\gamma)$ events at LEP2. Hadronic events in which a Z is accompanied by initial state photon radiation (ISR) are then removed in a procedure with several steps. First, ISR photons observed in the detector are identified as follows. The particles in the event are clustered into jets using the Durham algorithm [8] with a resolution parameter $y_{\rm cut}$ of 0.002. Jets where the fraction of the jet energy carried by charged hadrons is less than 10% are identified as dominantly electromagnetic if either less than half of the neutral energy is hadronic or there are no charged hadrons. From these 'electromagnetic jets', the γ and $\mathrm{e^+e^-}$ candidates are removed, assuming that they originate from an ISR process. These electrons and positrons are often the result of photon conversion in the material of the tracking chambers. Next, the remaining particles are clustered into two jets. The visible invariant mass $M_{\rm vis}$ of these two jets is determined and the reduced centre-of-mass energy s' is evaluated from the jet directions and total momentum conservation. The events with a large ISR energy component are rejected by requiring $M_{\rm vis}/\sqrt{s}$ to be larger than 0.7 or s'/s to exceed 0.81. According to Monte Carlo studies, the contamination from radiative events in the selected sample is about 4% at 206 GeV.

The events passing the anti-ISR cuts still contain background from four-fermion processes (WW, ZZ, $\mathrm{Z}\gamma^*$). These are identified by first clustering the particles to exactly four jets with the Durham algorithm. The energies of the jets are then rescaled, keeping their directions constant, such that the total energy of the event is equal to $E_{\rm cm}$ and the total momentum is zero. The quantities

$$d^2 = \min\left[\frac{(m_{ij} - M_{\rm W})^2 + (m_{kl} - M_{\rm W})^2}{M_{\rm W}^2}\right],$$

with M_{W}= 80.4 GeV/c^2, and

$$c_{\mathrm{W}} = \cos(\text{smallest interjet angle}) ,$$

are then computed. For d^2, the minimum value is taken among all possible choices of jet pairings ij and kl. Events are accepted as $\mathrm{q\overline{q}}$ events if $d^2 \geq 0.1$ or $c_{\mathrm{W}} \geq 0.9$.

2.3 The Data Sample and Detector Corrections

The integrated luminosities and numbers of accepted events at higher energies are given in Table 1. The event yields are compared to expected numbers of signal and background events. Signal events have been simulated with the program KORALZ [9], those for the WW background with KORALW [10] and for the ZZ and Zγ^* backgrounds with PYTHIA [11]. The expected background is subtracted from the distributions. The data taken at

Table 1: Integrated luminosities and numbers of accepted and expected events. The uncertainty in the predicted numbers of events is 2%.

E_{cm} (GeV)	$\int L\,dt$ (pb^{-1})	Events found	Events expected	Expected signal	Expected background
133	12.41	806	822	822	0
161	11.08	319	333	319	14
172	9.54	257	242	218	24
183	56.83	1319	1262	1109	153
189	174.36	3578	3578	3124	454
200	208.01	3514	3528	3005	523
206	216.19	3578	3590	3072	518

130 and 136 GeV are averaged into a single data set at a nominal energy of 133 GeV. Weights proportional to the luminosity are applied and distributions are corrected to 133 GeV. The same procedure is followed for the data sets at 196, 200 and 202 (averaged to $\sqrt{s}$= 200 GeV) and to the data taken in the range from 203 to 209 GeV (averaged to $\sqrt{s}$=206 GeV). The data are corrected for acceptance, detector resolution, undetected particles such as neutrinos, particle masses, final state photon radiation and the residual effects of ISR by means of multiplicative factors. The detector corrections in this paper are derived with KORALZ because of its more accurate description of ISR. These factors are observed to be practically independent of the model used. For the simulation of hadronic final states in e$^+$e$^-$ annihilation, PYTHIA and KORALZ are essentially equivalent.

The experimental systematic uncertainty related to the detector is estimated using calibration data collected at the Z peak in the same year as the high-energy data. The cuts on track parameters are changed in the simulated samples until the number of events selected per unit luminosity is the same in simulation and data. These modified cuts are then applied to the simulated high-energy events, and the change in the extracted values for each event-shape variable is taken as a systematic uncertainty.

The event-shape variables are measured using energy-flow objects. To account for imperfections in the description of neutral objects in the range from 1 to 2 GeV, these objects are excluded from the analysis, and the change in the resulting distribution is taken as systematic uncertainty. Systematic tests of the ISR and WW rejection and the event selection cuts are performed via cut variations. The dominant uncertainty is found to be related to the Monte Carlo description of ISR, which appears in the variation of cuts in $M_{\rm vis}$ and s'/s. All other cut variations lead to small uncertainties. The systematic uncertainty due to the residual model dependence of detector corrections is estimated by comparing with the results based on factors derived from HERWIG 6.1 [12] and from ARIADNE 4.1 [13]. Variations in the WW cross section used for background subtraction by ± 2 % lead to negligible uncertainties in the corrected distributions.

In the event-shape distributions, the systematic uncertainty estimates in each bin are dominated by the small changes in the selected events and tracks as cuts are varied, and hence are very much limited in statistical precision. For this reason, the estimates for neighbouring bins are combined in groups of three.

For the measurements at the Z peak, about 1.1 million events of highest quality corresponding to 41.48 pb^{-1} are selected from the running periods in 1994 and 1995. Because statistics are not an issue at LEP1, very stringent quality cuts are applied and earlier data are not considered. Event shapes and the logarithmic scaled momentum variable (Section 3) are reanalysed here, superseding a previous measurement presented in [1]. The distributions are corrected by means of a matrix method, as described in [1]. The experimental systematic uncertainties are obtained in a similar way to that at LEP2. The dominant experimental systematic uncertainties stem from the residual model dependence of detector corrections and from the imperfections of the simulation of neutral energy-flow objects in the range from 1 to 2 GeV.

3 Inclusive Charged Particle Distributions

Observables based on charged particles are measured for all data sets of Table 1. For inclusive charged particle measurements, which are less sensitive to statistical fluctuations, the data at 196 GeV (79.86 pb^{-1}) are analysed separately. Inclusive distributions are measured for the following variables.

- The scaled particle momentum, $x_p = 2p/\sqrt{s}$.
- The logarithmic representation of the scaled momentum, $\xi = -\ln x_p$, used to study the low momentum region.
- The scaled particle energy, $x_E = 2E/\sqrt{s}$.
- The momentum projection in the event plane transverse to the sphericity axis, $p_\perp^{\rm in}$. The event plane is defined by the sphericity and semi-major axes.
- The momentum transverse to the event plane, $p_\perp^{\rm out}$.
- The rapidity, $y_T = \frac{1}{2}\ln(E+p_{||})/(E-p_{||})$, measured with respect to the thrust axis.
- The rapidity, y_S, measured with respect to the sphericity axis.

The thrust and sphericity axes used for the rapidities and the event plane used for $p_\perp^{\rm in}$ and $p_\perp^{\rm out}$ are determined using both charged and neutral particles. Inclusive distributions of x_p and ξ are shown in Fig. 1, and of $p_\perp^{\rm in}$, $p_\perp^{\rm out}$, y_T and y_S in Fig. 2, at $\sqrt{s}$ = 206 GeV for illustration. The distributions of x_E, which are very similar to those of x_p except at very low x_E, are presented in Section 3.3. Numerical values in tabulated format and figures of the distributions at all energies can be obtained through the Durham HEP database [14] or from the ALEPH QCD web site [3]. The data are corrected for initial and final state photon radiation, detector effects and background. Corrected distributions are compared to the predictions of the models PYTHIA, HERWIG and ARIADNE. All three models have been tuned to the ALEPH data at LEP1 [1]. Overall, the generator predictions agree well with the data, except for $p_\perp^{\rm out}$. At all energies the spectrum of $p_\perp^{\rm out}$ is significantly harder and none of the generators describes the data correctly at large values. It also is the only variable for which a sizable difference between the models is observed.

3.1 Mean Charged Particle Multiplicity

The mean multiplicity of charged particles, $\langle N_{\rm ch}\rangle$, is among the observables most sensitive to the dynamics of hadron production. A model dependence arises because of the small

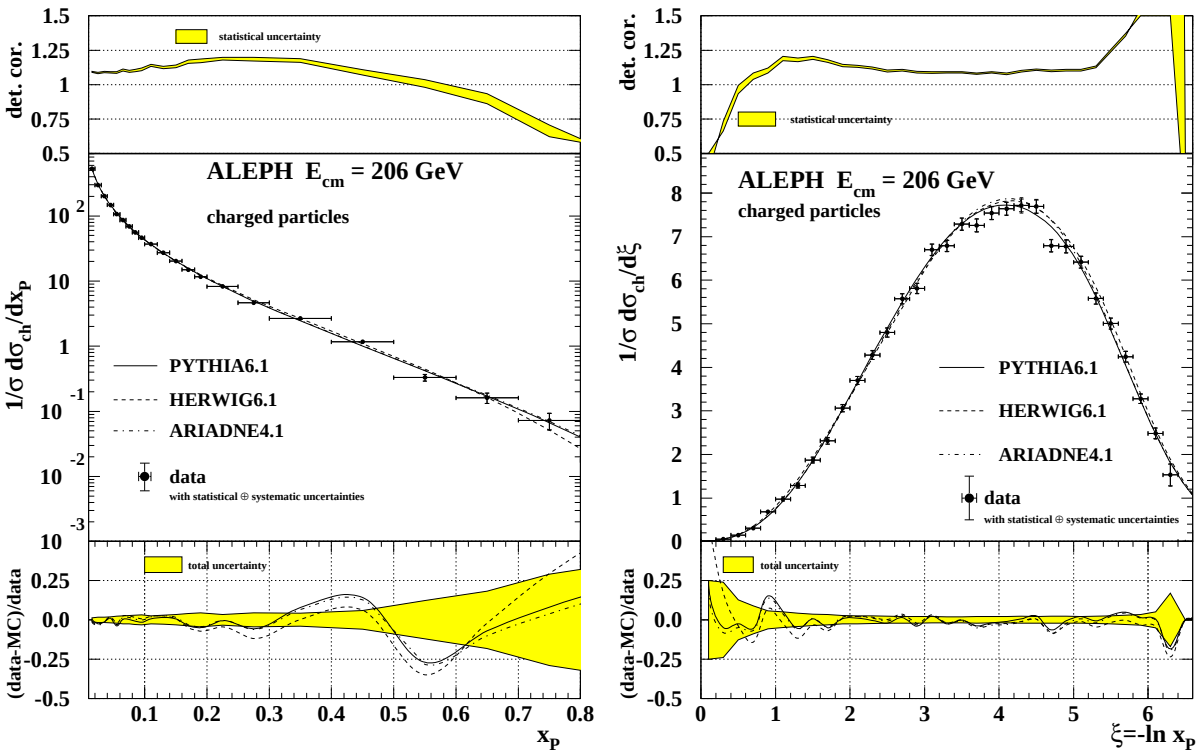

Figure 1: The measured inclusive charged particle distributions, after correction for backgrounds and detector effects, of $x_p = p/p_{\rm beam}$ and $\xi = -\ln x_p$ at $\sqrt{s}$=206 GeV are shown in the central parts of the plots. The top insets give the detector correction factors and the bottom insets the normalised differences with respect to the predictions of PYTHIA, HERWIG and ARIADNE.

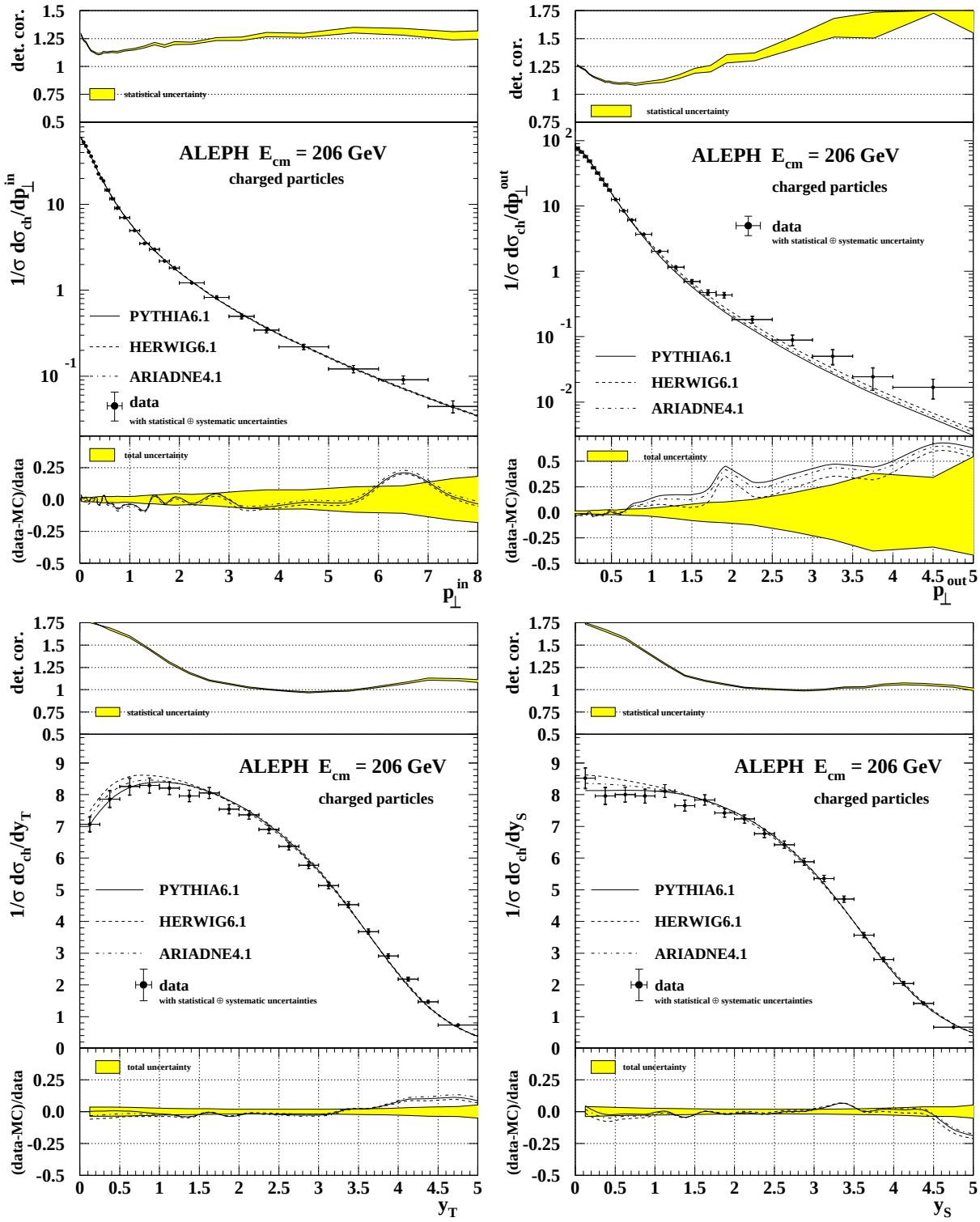

Figure 2: The measured inclusive charged particle distributions, after correction for backgrounds and detector effects, of $p_\perp^{\rm in}$, $p_\perp^{\rm out}$, rapidity with respect to the thrust (y_T) and to the sphericity axis (y_S) at $\sqrt{s}$ =206 GeV.

detection efficiency at low momenta. To alleviate this model dependence, $\langle N_{\rm ch}\rangle$ is obtained by integrating the rapidity distribution y_T. The results are given in Table 2. The experimental systematic uncertainties are obtained as outlined in Section 2. At LEP2 an average of the systematic uncertainties is calculated using weights proportional to the luminosity in order to smooth statistical fluctuations. Integrating variables other than y_T yields consistent results for $\langle N_{\rm ch}\rangle$. The differences are much smaller than the systematic uncertainty. The multiplicities measured at various centre-of-mass energies are shown in Fig. 3 along with measurements from other experiments [15] and with the predictions of the Monte Carlo models PYTHIA, HERWIG and ARIADNE.

Table 2: Mean charged particle multiplicity at different centre-of-mass energies.

$E_{\rm cm}$ [GeV]	$\langle N_{\rm ch}\rangle$	stat. error	syst. error
91.2	20.73	$\pm$ 0.01	$\pm$ 0.21
133	24.34	$\pm$ 0.38	$\pm$ 0.22
161	26.91	$\pm$ 0.58	$\pm$ 0.22
172	26.72	$\pm$ 0.62	$\pm$ 0.22
183	26.80	$\pm$ 0.35	$\pm$ 0.22
189	27.35	$\pm$ 0.22	$\pm$ 0.22
196	27.41	$\pm$ 0.33	$\pm$ 0.22
200	27.53	$\pm$ 0.29	$\pm$ 0.22
206	27.95	$\pm$ 0.22	$\pm$ 0.22

Also shown in Fig. 3 is a QCD prediction for the evolution of $\langle N_{\rm ch}\rangle$. Basic properties of particle production by multi-gluon emission emerge at leading order already, as given by the double logarithmic approximation (DLA). Colour coherence and gluon interference phenomena are better described in the modified leading logarithmic approximation (MLLA) [16] which incorporates single logarithmic corrections to the DLA. For the most inclusive variable $\langle N_{\rm ch}\rangle$ a next-to-next-to-next-to-leading order (3NLO) prediction exists [17] which takes recoil effects and conservation laws into account. The expansion parameter of these perturbation series is $Y = \ln Q/2Q_0$ where $Q = \sqrt{s}$ and Q_0 is a cut-off scale limiting the perturbative shower evolution. In the case of the *limiting spectrum* [16] the cut-off scale is set equal to the effective QCD scale, $Q_0 = \Lambda$. The effective scale in this scheme is not the same as in the $\overline{\rm MS}$ scheme. The concept of local parton-hadron duality (LPHD) allows the calculated parton multiplicities to be rescaled by a global normalisation factor, $K_{\rm LPHD}$, to obtain the observable hadron multiplicities.

Three different predictions are fit to the data. Expressions for the fit functions are given in Appendix A1 which contains the equations cited in the following paragraph. The simplest MLLA prediction is the *asymptotic* high-energy approximation Eq.(A1.1), valid only for large Y. The full MLLA prediction is obtained in the context of the limiting spectrum, Eq.(A1.2). The third prediction is the 3NLO calculation, Eq.(A1.3). In all cases two free parameters are fit, the QCD scale Λ and the normalisation $K_{\rm LPHD}$. The predictions depend on the number of flavours n_f for which two different scenarios are assumed: first, a pure light-quark assumption with n_f=3, and second, a more realistic frame with n_f=5 with a correction function for heavy quark decay dynamics applied to

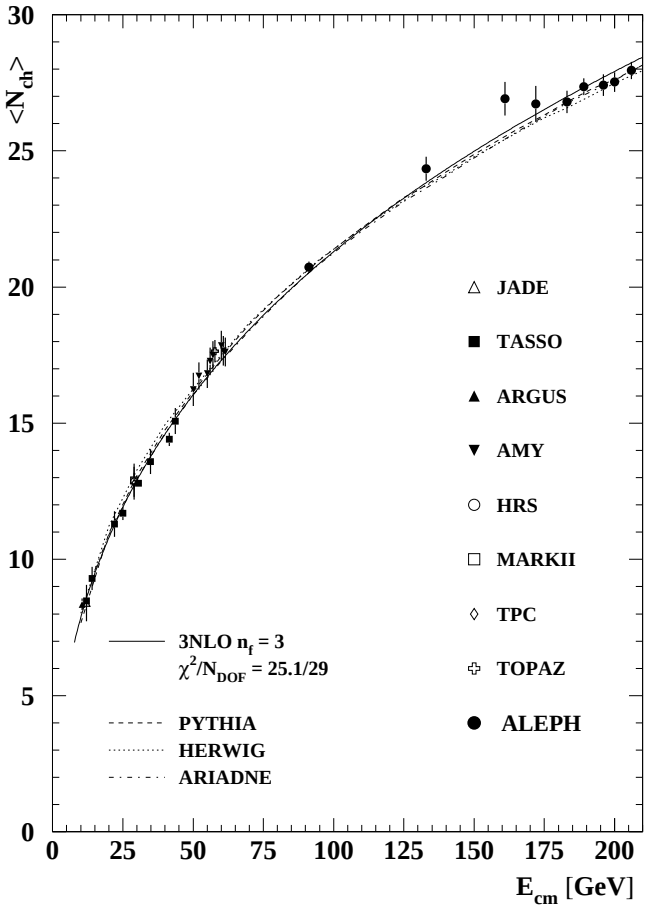

Figure 3: The mean charged particle multiplicity $\langle N_{\rm ch}\rangle$ as a function of centre-of-mass energy $E_{\rm cm}$. The measurements are compared to Monte Carlo predictions and to a fit of the QCD 3NLO evolution.

the perturbative predictions. The heavy quark correction is the multiplicity ratio for all flavours to uds quarks only and is obtained from Monte Carlo simulation at several centre-of-mass energies. The correction takes the energy-dependent flavour composition into account. The results of the various fits are listed in Table 3. The 3NLO curve shown in Fig. 3 corresponds to the best fit with $n_f = 3$. The other predictions and the inclusion of flavour correction yield an equally good description of the data. The corresponding curves cannot be distinguished from that for 3NLO. The data are also well described by the Monte Carlo models.

3.2 Distribution and Peak Position of ξ

The equations cited in this section are those in Appendix A2. The variable ξ is particularly sensitive to coherence phenomena in multiple gluon radiation. The suppression of hadron production at very small x (large ξ) is a consequence of the destructive interference of soft gluons.

3.2.1 Distributions

The distribution of ξ can be approximated by a Gaussian shape at asymptotically high energies. The MLLA corrections to the spectrum, which include the resummation of single and double logarithmic terms, have been calculated in [16]. Two predictions are used in

Table 3: Fits of different theoretical predictions to the mean charged particle multiplicity. The data points used are those in Fig. 3, which include statistical and experimental systematic uncertainties.

	n_f=3, no flavour correction			n_f=5, with flavour correction		
	Λ	K_{LPHD}	χ^2/N_{DOF}	Λ	K_{LPHD}	χ^2/N_{DOF}
asymptotic Eq.(A1.1)	557 ± 58	0.272 ± 0.011	26.1/29	178 ± 22	0.081 ± 0.004	30.2/29
lim. spect. Eq.(A1.2)	57 ± 7	0.587 ± 0.031	25.3/29	47 ± 6	0.481 ± 0.027	30.4/29
3NLO Eq.(A1.3)	207 ± 29	0.237 ± 0.013	25.1/29	202 ± 31	0.188 ± 0.012	30.8/29

this paper in addition to the normal Gaussian (Appendix A2). First, the prediction of the limiting spectrum, Eq.(A2.1), which depends on K_{LPHD}, Λ and n_f as is the case for $\langle N_{\mathrm{ch}} \rangle$ in Section 3.1. The second prediction is the *distorted Gaussian*, Eq.(A2.2), which includes higher-moment corrections to the Gaussian form. The distorted Gaussian prediction, introduced by Fong and Webber [18], depends on three parameters: an overall normalisation N_0, the scale Λ and an additive correction of order unity ($\mathcal{O}(1)$) to the mean value of ξ. As an example, fits at 189 GeV are shown in Fig. 4. In general the data are best described by the distorted Gaussian, in particular at large ξ, while the limiting spectrum reproduces the low ξ region better. All predictions provide a reasonable description of the peak region.

The limiting spectrum is highly predictive, and spectra at different energies can be fit simultaneously with two energy-independent parameters. A global fit to all energies yields $\Lambda = 247 \pm 3$ MeV and $K_{\mathrm{LPHD}} = 0.714 \pm 0.003$, with a poor fit quality $\chi^2/N_{\mathrm{DOF}} = 1204/102$. About half of the contribution to the χ^2 stems from the very precise Z peak data. At the individual energy points, the parameters range from 220 to 250 MeV for Λ and from 0.64 to 0.72 for K_{LPHD}.

For the distorted Gaussian prediction, each energy point has to be analysed separately, since the normalisation and the correction to the mean are energy dependent. The values for Λ range from 80 to 150 MeV and for the $\mathcal{O}(1)$ correction from -1.8 to -1.1.

3.2.2 Peak Position

The analytic fits to the spectra are used to determine the position of the peak of the distribution, denoted by ξ^*. Results are given in Table 4 using the distorted Gaussian which describes the data best.

The weighted average is calculated for the experimental systematic uncertainties above 91.2 GeV, as is done for $\langle N_{\mathrm{ch}} \rangle$. The nominal fit range used is the full width at a fraction

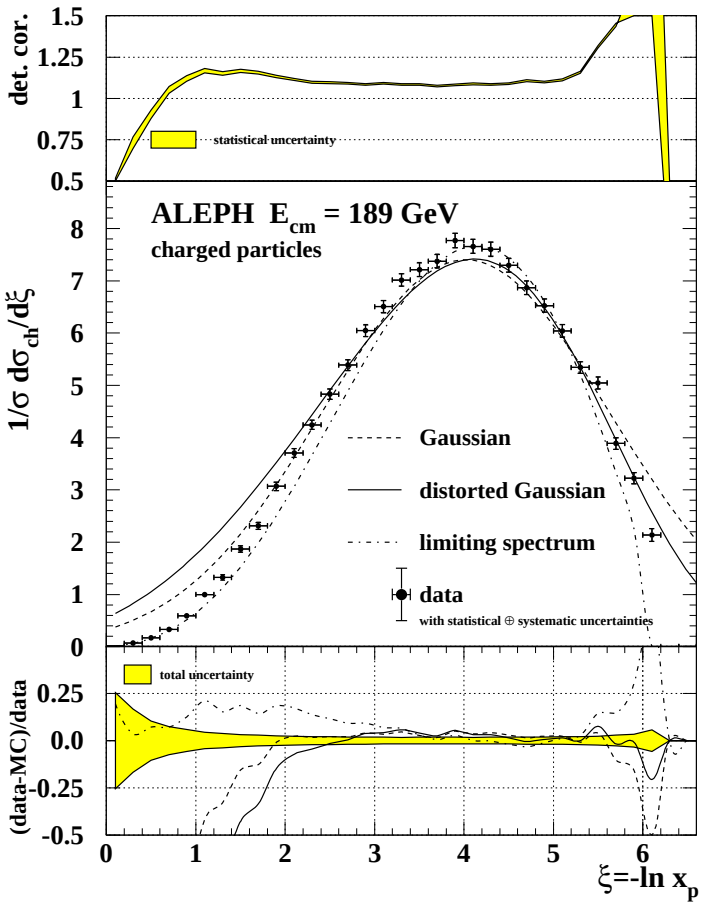

Figure 4: The spectrum of ξ at 189 GeV compared to different MLLA predictions described in the text. The upper inset shows detector corrections; the lower inset shows normalised residuals.

f = 70% of the maximum. An additional uncertainty not included in Table 4 arises from the choice of the fit range and is determined by varying the fraction f from 50% to 90%. This entails a coherent shift at all energies of the peak position of +0.020 for f = 50% to −0.016 for f = 90%, so that a correlated symmetric systematic uncertainty of ± 0.018 is assigned. Another systematic uncertainty is related to the choice of the fit function. Fitting the ξ distribution with a normal Gaussian results in a large correlated shift of +0.064 [1]. The peak position determined with the limiting spectrum is in better agreement with the distorted Gaussian and has a correlated shift of +0.014 relative to it. The total correlated systematic uncertainty for ξ^* is ±0.023, which is the quadratic sum of the components just discussed related to the fit range and to the fit function.

Within the framework of MLLA the energy evolution of ξ^* is predicted [16]. The formula Eq.(A2.4) depends only on Λ and is fit to the present data and measurements at lower energy [19] which have been determined using the same method [1] as here. The result is shown together with the data in Fig. 5. The evolution analysis is performed for a light quark assumption with n_f=3 and for a five-flavour case with n_f=5, as is done in Section 3.1 for $\langle N_{\rm ch}\rangle$. The peak position for events with b and c quarks is slightly shifted compared to light quark events. Therefore, the method of energy dependent flavour corrections derived from Monte Carlo simulation, as for $\langle N_{\rm ch}\rangle$, is applied to the fit procedure. The smallest $\chi^2/N_{\rm DOF}$ is obtained for n_f=3 and is presented in Fig. 5. The quality of the fit is good, $\chi^2/N_{\rm DOF}$ = 8.7/12, and Λ = 207 ± 8 MeV. With n_f=5 and

Table 4: Peak position ξ^* obtained with the distorted Gaussian fit to the ξ distribution at different centre-of-mass energies. The symbols $\Delta\xi^*_{\rm stat}$ and $\Delta\xi^*_{\rm exp}$ indicate the statistical and experimental systematic uncertainties.

Energy (GeV)	Fit range	$\xi^* \pm \Delta\xi^*_{\rm stat} \pm \Delta\xi^*_{\rm exp}$	Number of points	$\chi^2/N_{\rm DOF}$
91.2	[2.2,4.8]	$3.660 \pm 0.001 \pm 0.016$	13	4.2
133	[2.4,5.2]	$3.941 \pm 0.028 \pm 0.021$	14	1.5
161	[2.6,5.4]	$4.050 \pm 0.036 \pm 0.021$	14	2.1
172	[2.6,5.4]	$4.035 \pm 0.049 \pm 0.021$	14	1.3
183	[2.6,5.6]	$4.116 \pm 0.024 \pm 0.021$	15	1.7
189	[2.6,5.4]	$4.071 \pm 0.016 \pm 0.021$	14	0.8
196	[2.6,5.4]	$4.137 \pm 0.023 \pm 0.021$	14	0.8
200	[2.6,5.4]	$4.155 \pm 0.023 \pm 0.021$	14	1.0
206	[2.6,5.4]	$4.127 \pm 0.019 \pm 0.021$	14	1.6

flavour corrections $\Lambda = 217 \pm 8$ MeV is found with a $\chi^2/N_{\rm DOF}$ of 9.3/12.

3.3 Energy Evolution of x_E Distributions

Scaling violation in fragmentation functions is a fundamental prediction of perturbative QCD and can be tested by measuring the inclusive distributions of x_E at different centre-of-mass energies. In the framework of the improved parton model the inclusive production of hadrons is given by a convolution of the fragmentation function $D^{\rm h}_{\rm q}(x, Q^2)$ with the partonic cross sections. The energy dependence of the fragmentation functions is described by the DGLAP [20] equations. In a dedicated ALEPH analysis [21] the evolution of fragmentation functions for different flavours and the gluon was used to determine α_s. Here a comparison of the data measured up to the highest energies with the results of global parametrisations of fragmentation functions is given. Global parametrisations have been obtained by various authors, KKP [22], BWFG [23] and K [24]. In all of these analyses a functional form for the fragmentation functions $D(x, Q_0^2) = N\, x^a\, (1-x)^b$ at some initial scale Q_0 is assumed. Then the functions are evolved at NLO to fit the data at the Z peak and at lower energies. The high energy data are not included in the global fits, thus a comparison of the parametrisations with the data is an important test of the validity of their evolution.

In Fig. 6a the data at all energies are shown along with the three theoretical predictions. The previously published data [21] are used for $\sqrt{s} = 91.2$ GeV. At sufficiently large $x_E > 0.1$ the parametrisations describe the data well, and all three predictions are very similar. At small x_E the KKP parametrisation tends to rise more steeply than is supported by the data. Both the BFGW and K parametrisations extrapolate well

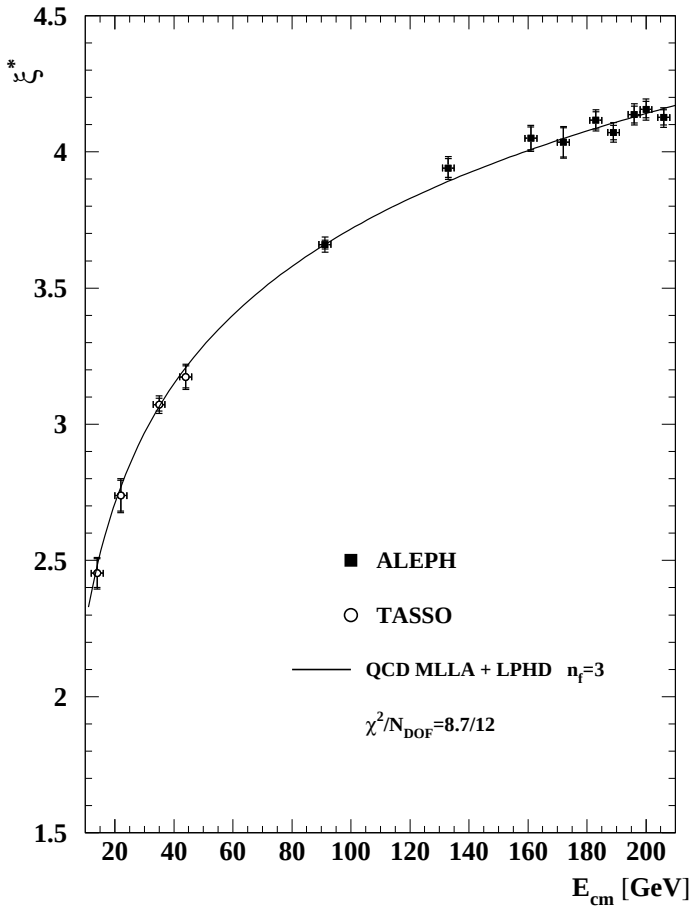

Figure 5: The peak position ξ^* as a function of centre-of-mass energy $E_{\rm cm}$. The inner error bars correspond to the uncorrelated experimental systematic uncertainty, the outer bars include the correlated component. The curve is a fit of the QCD MLLA evolution with n_f=3.

towards smaller x_E. In general the DGLAP mechanism does not apply for small x_E, where the MLLA formalism provides a better theoretical description, and this region is excluded from the global fits. In contrast, at very large x_E the KKP parametrisation is in better agreement with the data, while the BFGW and K parametrisations are below the measurements. However, the data at high x_E and at high energy are of limited precision. A striking consequence of scaling violations is observed in the ratio of the distributions at LEP2 and LEP1. The x_E spectra at the four highest energy data sets from 189 GeV to 206 GeV are combined in a luminosity-weighted average with a mean centre-of-mass energy of 198 GeV. The ratio of distributions is shown in Fig. 6b. Scaling violations induce a rise of the cross section at small x_E and at a decrease at large x_E with increasing $\sqrt{s}$. The data clearly exhibit this property, and it is qualitatively reproduced by the parametrisations; the predictions of the Monte Carlo models are in better agreement with the data.

4 Jet Rates

Jet rates are defined by means of the Durham clustering algorithm [8] in the following way. For each pair of particles i and j in an event the metric y_{ij} is computed

$$y_{ij} = \frac{2\min(E_i^2, E_j^2)(1-\cos\theta_{ij})}{E_{\rm vis}^2} ,$$

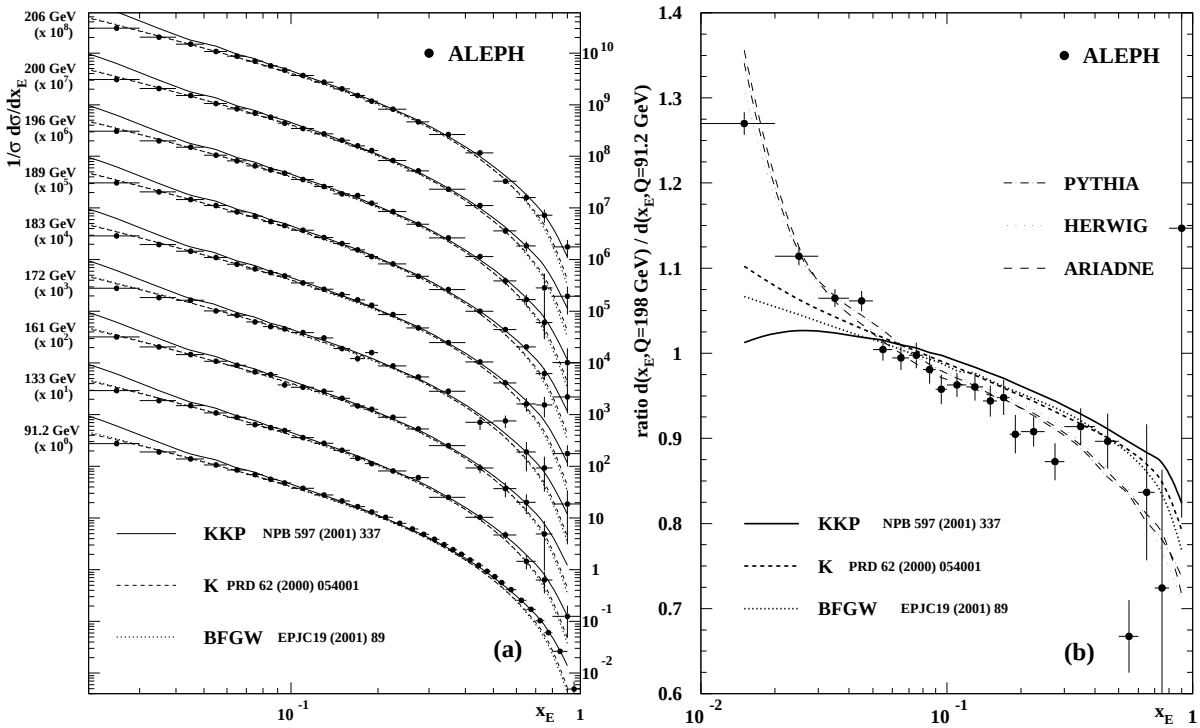

Figure 6: The inclusive scaled energy distributions compared to three different global NLO parametrisations of fragmentation functions (a). The ratio of the luminosity-weighted distribution at LEP2 (189-206 GeV, $\langle E_{\rm cm}\rangle$ =198 GeV) and 91.2 GeV, whereby the latter is taken from [21] (b).

where $E_{\rm vis}$ is the total visible energy in the event. The pair of particles with the smallest value of y_{ij} is replaced by a pseudo-particle (cluster). The four-momentum of the cluster is taken to be the sum of the four momenta of particles i and j, $p^\mu = p_i^\mu + p_j^\mu$ ('E' recombination scheme). The clustering procedure is repeated until all y_{ij} values exceed a given threshold $y_{\rm cut}$. The number of clusters remaining at this point is defined to be the number of jets. Alternatively, the procedure is repeated until exactly three clusters remain. The smallest value of y_{ij} in this configuration is defined as y_3. The distribution of y_3 is sensitive to the probability of hard gluon radiation leading to a three-jet topology. It can therefore be used to determine α_s (Section 6).

The n-jet rates were measured for $n = 1, 2, 3, 4, 5$ and $n \geq 6$. Detector correction factors were applied in the same manner as for the inclusive distributions, but in this case for each value of the jet resolution parameter $y_{\rm cut}$. Figure 7 shows the measured jet fractions as a function of $y_{\rm cut}$ at 206 GeV. Good agreement with the Monte Carlo generator predictions is observed. However, in the region of the peak of the three-jet fraction the generators, in particular PYTHIA, lie above the data.

5 Event Shapes

The various distributions describing the event shapes are of interest because *(i)* most of the variables are predicted to second order in QCD; and *(ii)* some resummed calculations

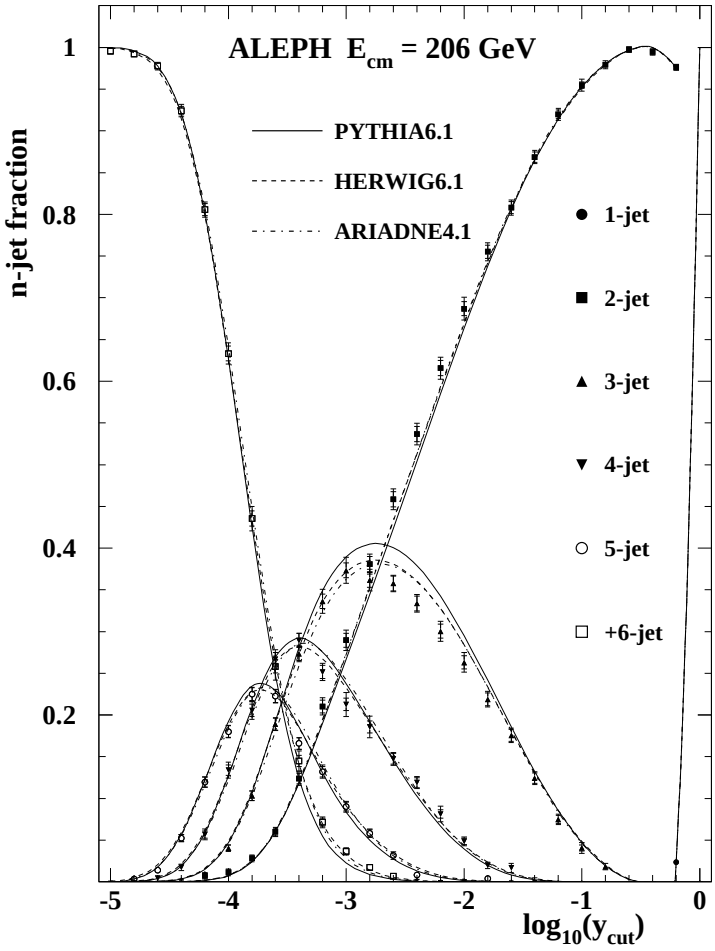

Figure 7: Measured n-jet fractions for $n = 1, 2, 3, 4, 5$ and $n \geq 6$ and the predictions of Monte Carlo models, at a centre-of-mass energy of 206 GeV.

to all orders in α_s exist. By fitting the theoretical predictions to these distributions the value of the strong coupling constant may be determined. By comparing with the direct predictions for the various Monte Carlo models, the validity of each model is tested.

The primary objective is to observe the running of α_s with centre-of-mass energy. For this reason, the analyses at each energy point have been carried out coherently and correlated systematic uncertainties are estimated. The event-shape variables studied here are defined as follows.

- Thrust $\boldsymbol{T}$: The thrust [25] axis $\vec{n}_T$ maximises the quantity

$$T = \max_{\vec{n}_T} \left(\frac{\sum_i |\vec{p}_i \cdot \vec{n}_T|}{\sum_i |\vec{p}_i|} \right) \quad ,$$

  where the sum extends over all particles in the event.

- Thrust Major $\boldsymbol{T}_{\mathbf{major}}$: The thrust major vector, $\vec{n}_{\mathrm{Ma}}$, is defined in the same way as the thrust vector, but with the additional condition that $\vec{n}_{\mathrm{Ma}}$ must lie in the plane perpendicular to $\vec{n}_T$,

$$T_{\mathrm{major}} = \max_{\vec{n}_{\mathrm{Ma}} \perp \vec{n}_T} \left(\frac{\sum_i |\vec{p}_i \cdot \vec{n}_{\mathrm{Ma}}|}{\sum_i |\vec{p}_i|} \right) \quad .$$

- Thrust Minor $\boldsymbol{T_{\mathrm{minor}}}$: The minor axis is perpendicular to both the thrust axis and the major axis, $\vec{n}_{\mathrm{Mi}} = \vec{n}_T \times \vec{n}_{\mathrm{Ma}}$. The value of thrust minor is given by

$$T_{\mathrm{minor}} = \frac{\sum_i |\vec{p}_i \cdot \vec{n}_{\mathrm{Mi}}|}{\sum_i |\vec{p}_i|} \quad .$$

- Oblateness $\boldsymbol{O}$: The oblateness is defined as the difference between thrust major and thrust minor,

$$O = T_{\mathrm{major}} - T_{\mathrm{minor}} \quad .$$

- Sphericity $\boldsymbol{S}$: The sphericity is calculated from the ordered eigenvalues $\lambda_{i=1,2,3}$ of the quadratic momentum tensor

$$\begin{aligned} M^{\alpha\beta} &= \frac{\sum_i p_i^\alpha p_i^\beta}{\sum_i |\vec{p}_i|^2} \quad , \ \alpha, \beta = 1, 2, 3 \quad ; \\ \lambda_1 &\geq \lambda_2 \geq \lambda_3 \quad , \ \lambda_1 + \lambda_2 + \lambda_3 = 1 \quad ; \\ S &= \frac{3}{2}(\lambda_2 + \lambda_3) \quad . \end{aligned}$$

  The sphericity axis $\vec{n}_S$ is defined along the direction of the eigenvector associated to λ_1, the semi-major axis $\vec{n}_{\mathrm{sMa}}$ is along the eigenvector associated to λ_2.

- Aplanarity $\boldsymbol{A}$: The aplanarity is calculated from the third eigenvalue of the quadratic momentum tensor,

$$A = \frac{3}{2}\lambda_3 \quad .$$

- Planarity $\boldsymbol{P}$: The planarity is a linear combination of the second and third eigenvalue of the quadratic momentum tensor

$$P = \lambda_2 - \lambda_3 \quad ,$$

  which is equivalent to the combination $P = \frac{2}{3}(S - 2A)$.

- Heavy Jet Mass $\boldsymbol{\rho}$: A plane through the origin and perpendicular to $\vec{n}_T$ divides the event into two hemispheres, H_1 and H_2, from which the corresponding normalised hemisphere invariant masses are obtained,

$$M_i^2 = \frac{1}{E_{\mathrm{vis}}^2} \left(\sum_{k \in H_i} p_k \right)^2 \quad , \ i = 1, 2 \quad .$$

  The larger of the two hemisphere masses is called the heavy jet mass [26],

$$\rho = \max(M_1^2, M_2^2) \quad ,$$

  and the smaller is the light jet mass M_L,

$$M_L = \min(M_1^2, M_2^2) \quad .$$

- Jet Mass Difference $\boldsymbol{M_D}$: The difference between ρ and M_L is called the jet mass difference,

$$M_D = \rho - M_L \ .$$

- Wide Jet Broadening $\boldsymbol{B_W}$: A measure of the broadening [27] of particles in transverse momentum with respect to the thrust axis can be calculated for each hemisphere H_i using the relation

$$B_i = \frac{\sum_{k \in H_i} |\vec{p}_k \times \vec{n}_T|}{2 \sum_j |\vec{p}_j|} \ , \ i = 1, 2 \quad ,$$

  where j runs over all of the particles in the event. The wide jet broadening is the larger of the two hemisphere broadenings,

$$B_W = \max(B_1, B_2) \ ,$$

  and the smaller is called the narrow jet broadening B_N,

$$B_N = \min(B_1, B_2) \ .$$

- Total Jet Broadening $\boldsymbol{B_T}$: The total jet broadening is the sum of the wide and the narrow jet broadenings,

$$B_T = B_W + B_N \ .$$

- C-parameter $\boldsymbol{C}$: The C-parameter [28] is derived from the eigenvalues of the linearised momentum tensor $\Theta^{\alpha\beta}$,

$$\Theta^{\alpha\beta} = \frac{1}{\sum_i |\vec{p}_i|} \sum_i \frac{p_i^\alpha p_i^\beta}{|\vec{p}_i|} \ , \ \alpha, \beta = 1, 2, 3 \ .$$

  The three eigenvalues λ_j of this tensor define C with

$$C = 3 \cdot (\lambda_1 \lambda_2 + \lambda_2 \lambda_3 + \lambda_3 \lambda_1) \ .$$

- Jet resolution parameter $\boldsymbol{y_n}$: The jet resolution parameters y_n are defined as the particular values of $y_{\rm cut}$ at which an event changes from a $(n-1)$-jet configuration to a n-jet configuration. The same clustering algorithm as for jet rates is applied.

Examples of observed data distributions for the selected events at 206 GeV, after correction for backgrounds and for detector effects, are shown in Fig. 8 and Fig. 9. On each plot detector correction factors and hadronisation corrections are displayed. The hadronisation corrections are defined as the ratio of the simulated distribution at hadron level to that at parton level. This correction is relevant for the comparison with analytic QCD calculations and the determination of α_s. The data distributions are compared with those predicted by PYTHIA, HERWIG and ARIADNE, at hadron level. The residuals of the model predictions with respect to the data are shown at the bottom of the plots. In the central part of the distributions the Monte Carlo predictions are in good agreement with the measurements and with each other. For some variables deviations are visible in the very two-jet region or in the multi-jet tail. Observables which are used for the determination of α_s are shown in Figs. 10 and 11. The measurements of all the event-shape distributions and mean values, including a large variety of additional variables measured at LEP1, are accessible at the ALEPH QCD web site [3].

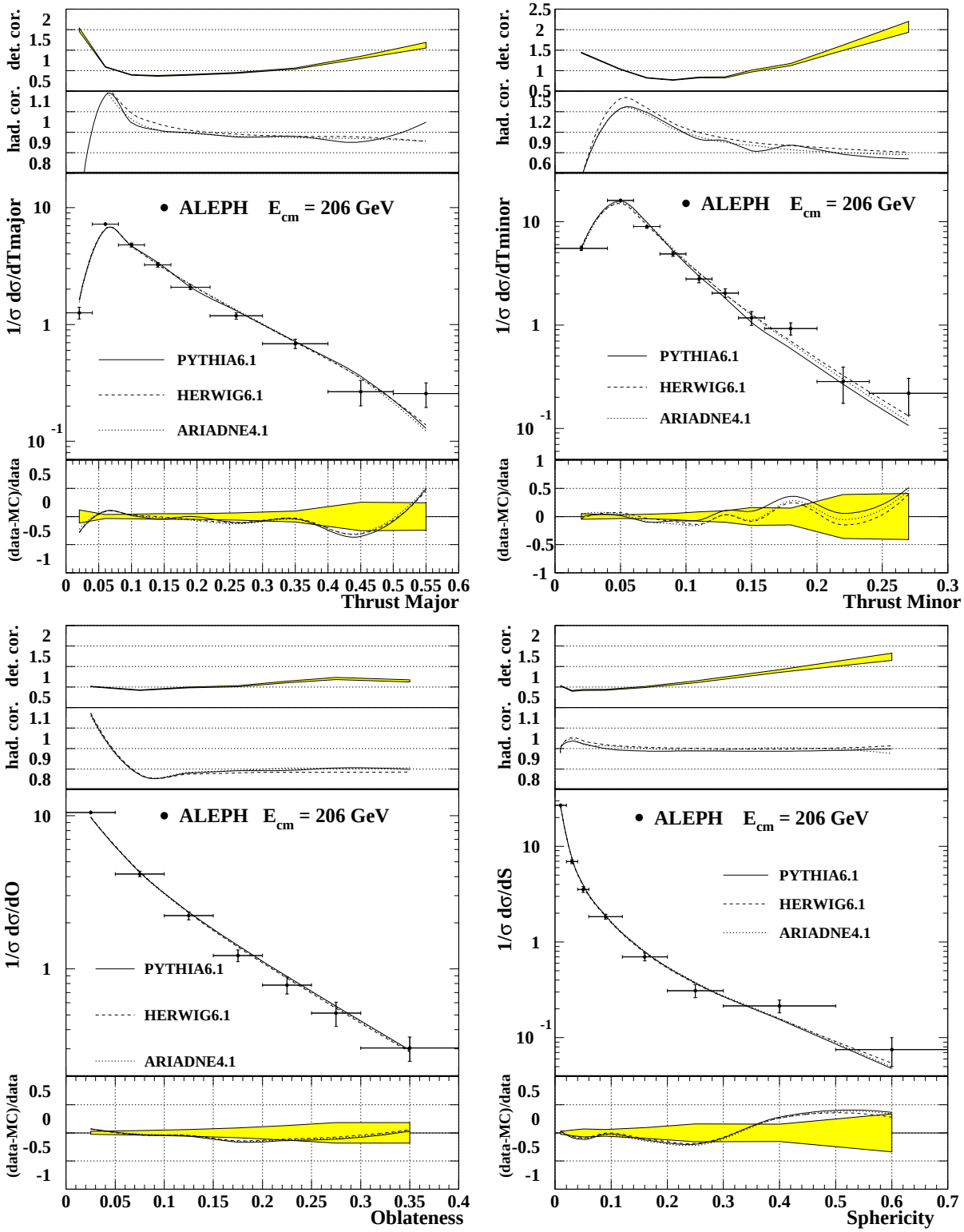

Figure 8: Corrected distributions of Major, Minor, Oblateness and Sphericity at $\sqrt{s}$ =206 GeV. The curves represent calculations using the QCD generators. The outer vertical error bars correspond to the quadratic sum of statistical and systematic uncertainties; the dominant statistical component is indicated by the inner error bars. The difference between them is hardly visible. The upper insets show detector correction factors and hadronisation corrections, the lower insets show the model residuals compared to the uncertainty envelope of the data in grey.

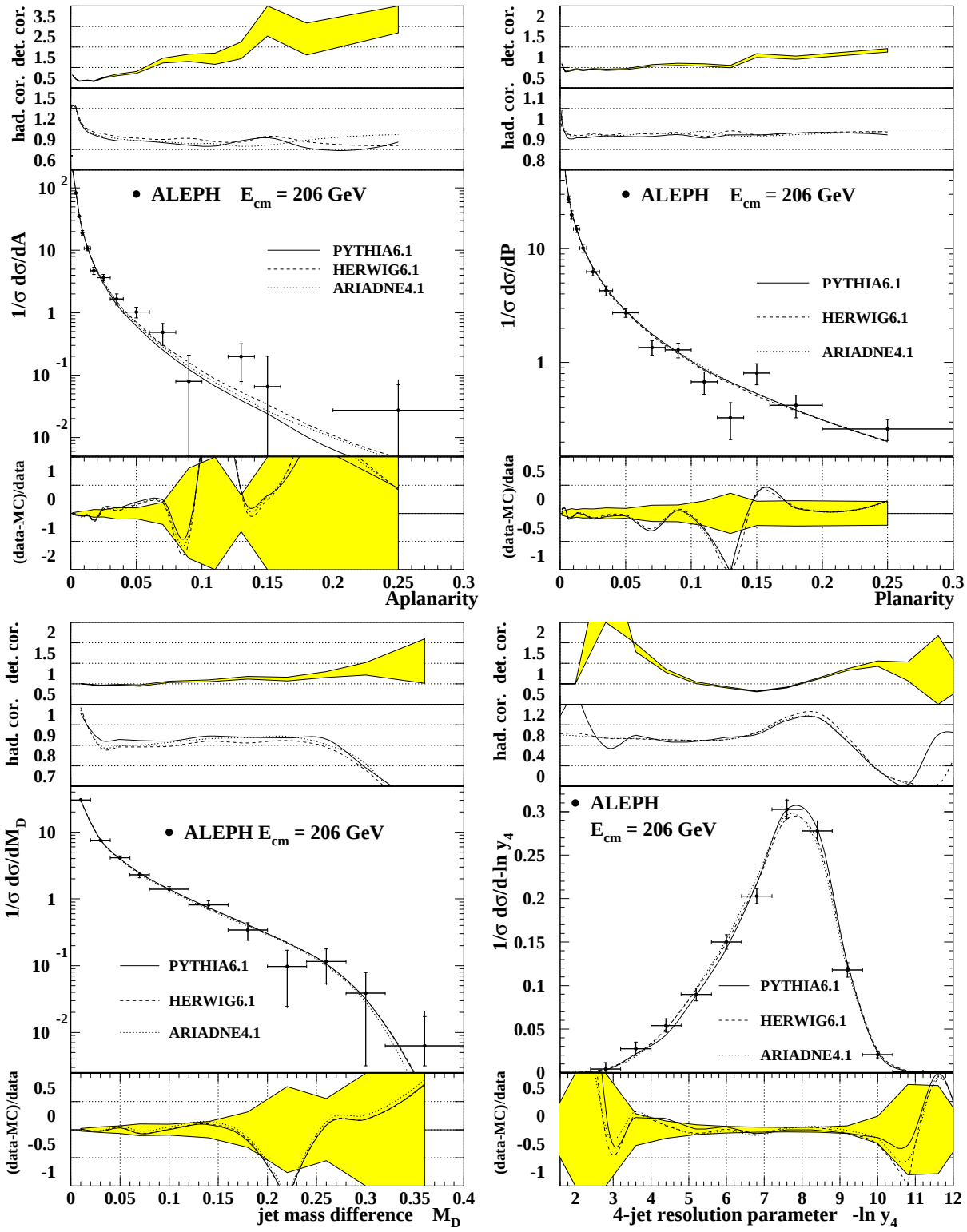

Figure 9: Corrected distributions of Aplanarity, Planarity, Jet Mass Difference and $-\ln y_4$ at $\sqrt{s}$=206 GeV. The curves represent calculations using the QCD generators. The outer vertical error bars correspond to the quadratic sum of statistical and systematic uncertainties; the dominant statistical component is indicated by the inner error bars. The difference between them is hardly visible. The upper insets show detector correction factors and hadronisation corrections, the lower insets show the model residuals compared to the uncertainty envelope of the data in grey.

6 Measurements of α_s

Distributions of event-shape variables are used to determine the strength of strong interactions. The coupling constant α_s is determined from a fit of the perturbative QCD prediction to measured event-shape distributions. The six event-shape variables used are T, ρ, B_T, B_W, C and $-\ln y_3$. Predictions for the distributions are calculated to the same order of perturbation theory for all of these variables. The size of missing higher orders, which are inherently difficult to assess, can be different for different variables. Therefore, a combination of measurements using several variables yields a better estimator of α_s than using a single variable. Furthermore the spread of values of α_s is an independent estimation of the theoretical uncertainty.

The experimental situation at energies above M_{Z} is different from that at M_{Z}. Statistical uncertainties are larger and background conditions are more difficult. In general theoretical uncertainties limit the precision of the measurements, except for the very small data sets at 161 and 172 GeV, where statistical errors dominate. At these energies it is particularly important to combine measurements from different variables.

A study using simulated distributions reveals that the fit procedure is systematically biased towards lower values of α_s in the case of small event statistics, as encountered at 161 and 172 GeV. This bias originates from larger weights of downward fluctuating bins in the distributions compared to upward fluctuations. It is overcome by replacing the measured statistical uncertainties of a distribution by the expected statistical errors. The expected uncertainties are obtained from a large number of simulated experiments, each of the same sample size as the real data. The root mean square in each bin of the Monte Carlo distributions is used in the fit procedure as statistical error. This is done for all variables at all energy points above M_{Z}.

Event-shape distributions are fit in a central region of three-jet production, where a good perturbative description is available. It extends from above the two-jet peak to the phase-space boundary between three and four jets. The fit range is placed inside the region where hadronisation and detector corrections are below 25% and the signal-to-background ratio is above one. The correction functions can be obtained at the ALEPH QCD web site [3]. Because of the large statistics at $Q = M_{\mathrm{Z}}$ this range extends well into the three-jet region. At high energies the range must be shifted into the two-jet region in order to reduce the statistical error and backgrounds as much as possible. This generates larger perturbative uncertainties, so that an iterative procedure is used to find the range giving the minimal total uncertainty. The data are corrected for detector effects, for background from four-fermion processes and for a residual ISR contribution, as outlined in Section 2. The background from WW events increases with energy, and after subtraction the content of some bins of the distribution becomes negative. For this reason the fit range is restricted to a region with good signal-to-background ratio.

Distributions of infrared- and collinear-safe observables at the parton level can be computed in perturbative QCD to second order in α_s using the ERT matrix elements [29]. In addition, the variables used in this analysis exhibit the property of exponentiation so that leading and next-to-leading logarithms can be resummed to all orders in α_s using analytic functions [30, 31, 32, 33]. These resummed calculations are valid in the semi-inclusive two-jet region, i.e., where the two jets are accompanied by multiple soft gluon radiation. An improved prediction over the entire phase space is achieved by

matching the fixed order part to the resummed calculation. For convenience, the main formulae are given in Appendix A3. A comprehensive overview can be found in [4]. The nominal value for the renormalisation scale $x_\mu = \mu/Q$ is unity. For this analysis *modified* versions of the Log(R) and R [30] matching schemes are used (Eqs.(A3.6), (A3.8), and (A3.12)). A kinematic constraint is imposed such that the predicted distributions of $y\,(y = 1-T, \rho, B_W, B_T, y_3, C)$ vanish at a given boundary value $y_{\max}$. Recently, improved calculations for $-\ln y_3$ have become available [34], which add previously missing single-logarithmic terms due to multiple gluon emission. The improved calculations have been implemented in the fit functions. It is observed that the quality of the fits to $-\ln y_3$ improves and the fitted value of α_s is 1.5% lower than the partial prediction [31].

All these calculations above neglect quark masses. Quark mass effects are relevant for the b quark at $\sqrt{s} = M_{\mathrm{Z}}$, where the fraction of $\mathrm{b\overline{b}}$ events is large, while Q is still moderate. Calculations including a quark mass indicate that the expected change in α_s is of the order of 1% at M_{Z} [35]. The effect is scaling with M_{b}^2/Q^2 and decreases to 0.2-0.3% at 200 GeV. Mass corrections were computed to second order using the matrix elements of [36]. A pole b-quark mass $M_{\mathrm{b}} = 5$ GeV/c^2 was used and Standard Model values were taken for the fraction of $\mathrm{b\overline{b}}$ events. Since no corrections are yet available for the resummed calculations, the full theoretical prediction can only account for the quark mass effect in the perturbative region.

The perturbative QCD prediction is corrected for hadronisation and resonance decays by means of a transition matrix, which is computed with Monte Carlo generators. Corrected measurements of event-shape distributions are compared to the theoretical calculation at particle level.

The value of α_s is determined at each energy using a binned least-square fit. Only statistical uncertainties are included in the χ^2 of the fit for which the quality is good for all variables at LEP2, while at LEP1 it is poor for the variables ρ and B_W. Nominal results are shown in Figs. 10 and 11 together with the measured distributions. The resulting measurements of $\alpha_s(Q)$ are given in Table 5 for 91.2 to 172 GeV and in Table 6 for 183 to 206 GeV. All individual measurements are also shown in Fig. 12 together with combined measurements at each energy (Section 8). Systematic theoretical and experimental uncertainties are discussed in the following section.

7 Systematic Uncertainties of α_s

7.1 Experimental Uncertainties

Experimental systematic uncertainties are estimated in a way similar to that for the event shapes themselves, as described in Section 2. Changes of the distributions under variations of cuts lead in general to small changes in α_s. In the fit procedure the same expected statistical error is assumed everywhere for all variants of the distribution, as outlined in Section 6. This procedure reduces purely statistical components in the systematic effect, which are potentially large at LEP2 energies. A special treatment was applied for the dominant systematic uncertainty, i.e. arising from the variation of the combined cut in $M_{\mathrm{vis}}/\sqrt{s}$ from 0.7 to 0.85 and in s'/s from 0.81 to 0.9. This cut variation entails the largest change in the number of events. The resulting error in α_s fluctuates from one

Table 5: Results on $\alpha_s(Q)$ as obtained from fits to distributions of event-shape variables at $\sqrt{s}$ = 91.2, 133, 161 and 172 GeV.

Q = 91.2 GeV						
variable	T	$-\ln y_3$	ρ	C	B_W	B_T
α_s	0.1264	0.1180	0.1187	0.1225	0.1163	0.1260
stat. error	0.0001	0.0002	0.0002	0.0001	0.0002	0.0001
exp. error	0.0008	0.0010	0.0009	0.0007	0.0006	0.0007
pert. error	0.0063	0.0038	0.0043	0.0058	0.0051	0.0080
hadr. error	0.0020	0.0015	0.0037	0.0015	0.0015	0.0029
total error	0.0067	0.0042	0.0057	0.0061	0.0054	0.0085
fit range	0.80-0.94	1.6-4.4	0.08-0.21	0.26-0.64	0.08-0.15	0.08-0.22
Q = 133 GeV						
variable	T	$-\ln y_3$	ρ	C	B_W	B_T
α_s	0.1196	0.1180	0.1141	0.1188	0.1143	0.1112
stat. error	0.0040	0.0054	0.0044	0.0029	0.0026	0.0022
exp. error	0.0012	0.0010	0.0010	0.0011	0.0004	0.0017
pert. error	0.0054	0.0030	0.0036	0.0049	0.0044	0.0068
hadr. error	0.0015	0.0008	0.0025	0.0012	0.0009	0.0019
total error	0.0069	0.0064	0.0063	0.0060	0.0052	0.0076
fit range	0.80-0.96	1.6-4.8	0.06-0.25	0.18-0.75	0.05-0.25	0.06-0.40
Q = 161 GeV						
variable	T	$-\ln y_3$	ρ	C	B_W	B_T
α_s	0.1214	0.1118	0.1178	0.1224	0.1159	0.1138
stat. error	0.0062	0.0084	0.0073	0.0046	0.0041	0.0040
exp. error	0.0012	0.0010	0.0010	0.0012	0.0004	0.0018
pert. error	0.0049	0.0027	0.0034	0.0045	0.0040	0.0062
hadr. error	0.0013	0.0006	0.0020	0.0011	0.0007	0.0015
total error	0.0081	0.0089	0.0083	0.0066	0.0058	0.0078
fit range	0.80-0.96	1.6-5.6	0.06-0.25	0.18-0.75	0.05-0.30	0.06-0.40
Q = 172 GeV						
variable	T	$-\ln y_3$	ρ	C	B_W	B_T
α_s	0.1122	0.1078	0.1087	0.1089	0.1040	0.1140
stat. error	0.0075	0.0093	0.0079	0.0055	0.0053	0.0056
exp. error	0.0012	0.0011	0.0010	0.0012	0.0005	0.0018
pert. error	0.0048	0.0027	0.0034	0.0045	0.0040	0.0060
hadr. error	0.0012	0.0005	0.0019	0.0010	0.0007	0.0014
total error	0.0091	0.0098	0.0088	0.0072	0.0067	0.0085
fit range	0.80-0.96	2.4-5.6	0.06-0.25	0.18-0.75	0.05-0.30	0.06-0.30

Table 6: Results on $\alpha_s(Q)$ as obtained from fits to distributions of event-shape variables at $\sqrt{s}$ =183, 189, 200 and 206 GeV.

Q = 183 GeV						
variable	T	$-\ln y_3$	ρ	C	B_W	B_T
α_s	0.1132	0.1058	0.1103	0.1079	0.1062	0.1148
stat. error	0.0035	0.0044	0.0038	0.0031	0.0025	0.0027
exp. error	0.0012	0.0012	0.0010	0.0013	0.0004	0.0018
pert. error	0.0048	0.0026	0.0032	0.0044	0.0038	0.0059
hadr. error	0.0011	0.0005	0.0018	0.0010	0.0006	0.0013
total error	0.0061	0.0053	0.0054	0.0056	0.0046	0.0079
fit range	0.80-0.96	2.4-5.6	0.06-0.20	0.22-0.60	0.05-0.20	0.075-0.25
Q = 189 GeV						
variable	T	$-\ln y_3$	ρ	C	B_W	B_T
α_s	0.1163	0.1080	0.1099	0.1124	0.1056	0.1140
stat. error	0.0021	0.0027	0.0028	0.0018	0.0016	0.0019
exp. error	0.0012	0.0010	0.0012	0.0012	0.0004	0.0019
pert. error	0.0046	0.0026	0.0032	0.0042	0.0038	0.0059
hadr. error	0.0011	0.0004	0.0017	0.0010	0.0006	0.0012
total error	0.0053	0.0039	0.0047	0.0049	0.0042	0.0065
fit range	0.84-0.96	2.4-5.6	0.06-0.16	0.22-0.60	0.05-0.20	0.075-0.20
Q = 200 GeV						
variable	T	$-\ln y_3$	ρ	C	B_W	B_T
α_s	0.1113	0.1091	0.1037	0.1113	0.1028	0.1141
stat. error	0.0023	0.0027	0.0034	0.0021	0.0019	0.0021
exp. error	0.0012	0.0010	0.0017	0.0012	0.0004	0.0018
pert. error	0.0045	0.0026	0.0031	0.0042	0.0037	0.0058
hadr. error	0.0011	0.0004	0.0016	0.0010	0.0005	0.0011
total error	0.0053	0.0039	0.0052	0.0049	0.0042	0.0065
fit range	0.84-0.96	2.4-5.6	0.06-0.16	0.22-0.60	0.05-0.20	0.075-0.20
Q = 206 GeV						
variable	T	$-\ln y_3$	ρ	C	B_W	B_T
α_s	0.1097	0.1024	0.1075	0.1052	0.1035	0.1076
stat. error	0.0023	0.0028	0.0029	0.0019	0.0016	0.0019
exp. error	0.0012	0.0010	0.0010	0.0012	0.0004	0.0018
pert. error	0.0045	0.0026	0.0031	0.0041	0.0037	0.0056
hadr. error	0.0011	0.0004	0.0016	0.0009	0.0005	0.0011
total error	0.0053	0.0039	0.0046	0.0048	0.0041	0.0063
fit range	0.84-0.96	2.4-5.6	0.06-0.16	0.22-0.60	0.05-0.20	0.075-0.20

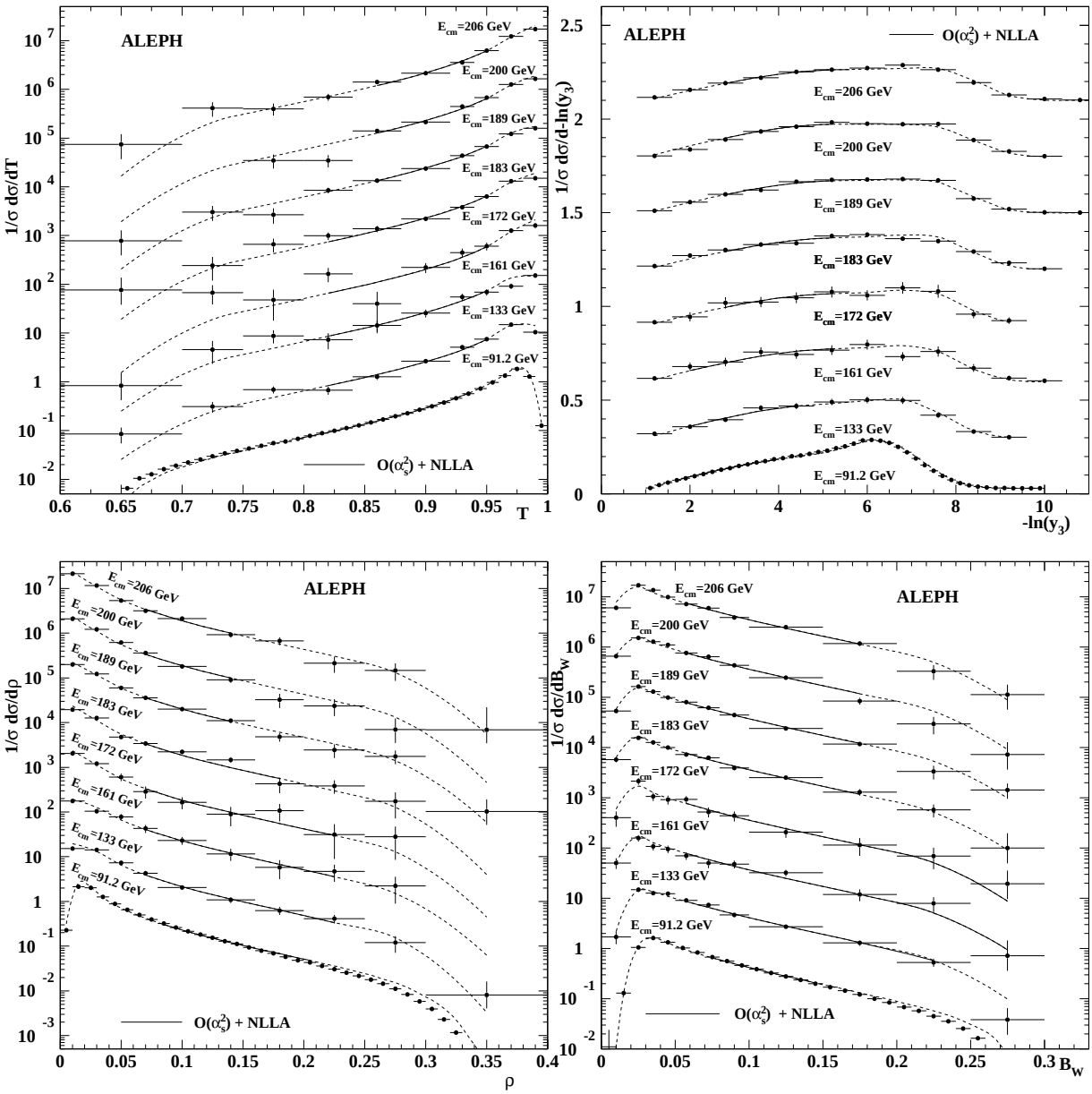

Figure 10: The measured distributions, after correction for backgrounds and detector effects, of thrust, $-\ln y_3$, heavy jet mass and wide jet broadening at energies between 91.2 and 206 GeV together with the fitted QCD predictions. The error bars correspond to statistical uncertainties. The fit ranges cover the central regions indicated by the solid curves, the theoretical predictions extrapolate well outside the fit ranges, as shown by the dotted curves. The plotted distributions are scaled by arbitrary factors for presentation.

energy to another due to the irreducible statistical component. Therefore, an energy-independent luminosity-weighted average is constructed for each variable separately at energies between 133 and 206 GeV. All other components of systematic uncertainty are added in quadrature to this error. The total experimental systematic uncertainties of α_s at LEP2 are between 0.5% and 1.5%. Those at LEP1 are below 1% and dominated by

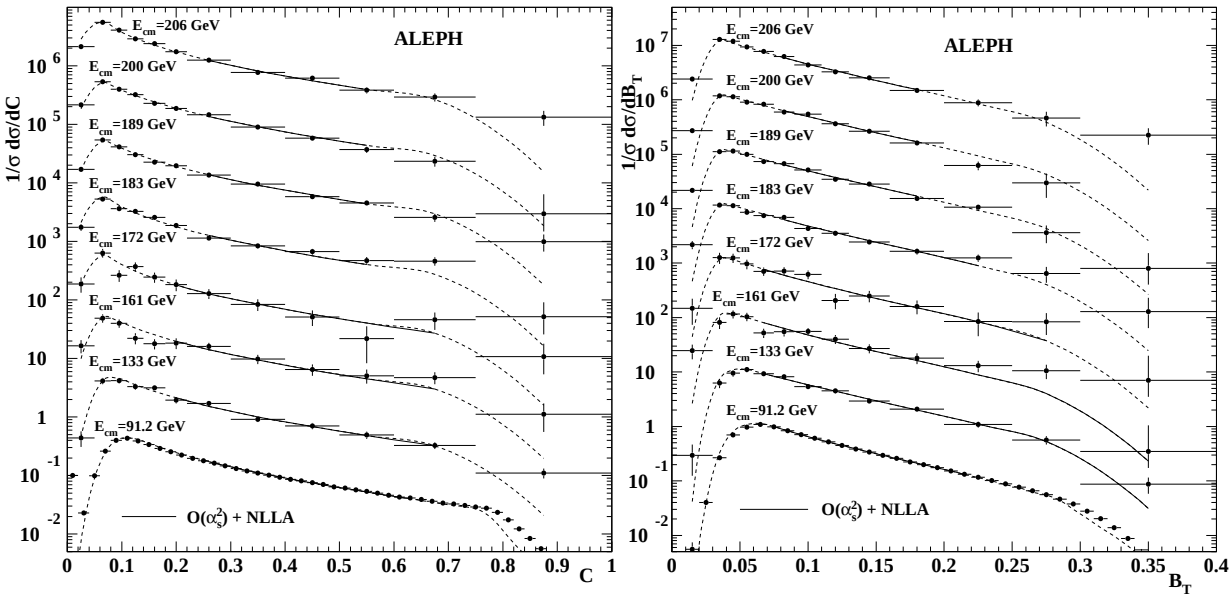

Figure 11: The measured distributions, after correction for backgrounds and detector effects, of C-parameter and total jet broadening at energies between 91.2 and 206 GeV together with the fitted QCD predictions. The error bars correspond to statistical uncertainties. The fit ranges cover the central regions indicated by the solid curves, the theoretical predictions extrapolate well outside the fit ranges, as shown by the dotted curves. The plotted distributions are scaled by arbitrary factors for presentation.

imperfections of the simulation of neutral hadronic energy-flow objects.

7.2 Theoretical Uncertainties

The new method recommended in [4] is applied to estimate systematic uncertainties related to missing higher orders. Sources of arbitrariness in the predictions are the choice of the renormalisation scale x_μ and the logarithmic rescaling factor x_L, the matching scheme and the matching modification procedure. For the logarithmic rescaling factor an additional test, first suggested in [37], is included here. Essentially this test consists in a replacement of the logarithmic variable $L = -\ln y$ (y being an event shape variable such as $1-T$), by a rescaled variable $L \to \widehat{L} = -\ln(y \cdot x_L)$ with x_L of order unity. A variation of x_L is expected to probe missing higher orders in a way different from renormalisation scale variations. Values of x_L different from unity entail changes of the matching formulae, given in Appendix A3. The so-called perturbative uncertainties are assessed as follows:

- the renormalisation scale x_μ is varied between 0.5 and 2.0,
- the logarithmic rescaling factor x_L varied in between 2/3 and 3/2 (for $-\ln y_3$ an equivalent effect is obtained with the endpoints squared, i.e., a variation from 4/9 to 9/4),
- the modified Log(R) matching scheme is replaced by the modified R matching scheme,

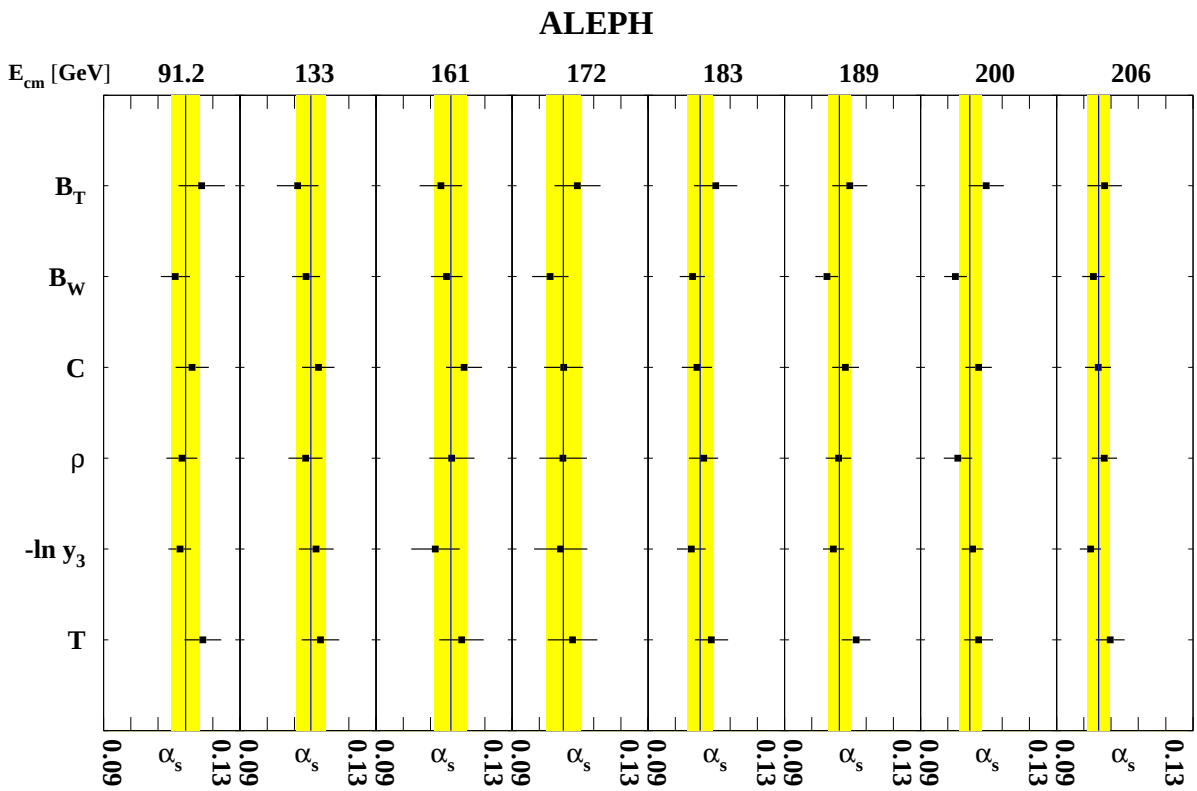

Figure 12: Summary of all individual measurements of α_s using six variables at eight centre-of-mass energies. The error bars correspond to the total uncertainties, the shaded areas to the combined measurements given in Table 7.

- the value of the kinematic constraint $y_{\max}$, obtained with parton shower simulations, is replaced by the value of $y'_{\max}$ using matrix element calculations and
- the first degree modification of the modified Log(R) matching scheme ($p = 1$) is replaced by a second degree modification ($p = 2$).

The uncertainties in α_s corresponding to these theoretical uncertainties were previously obtained by modifying the prediction (e.g., setting a different value of x_μ), and repeating the fits to the data. The quality of fits carried out with extreme variations of theoretical predictions is usually rather bad, and the values for parameters determined under such conditions are less reliable.

The new method derives the uncertainty of α_s from the uncertainty of the theoretical prediction for the event-shape distribution and proceeds in three steps. First a reference perturbative prediction, the modified Log(R) matching scheme, is determined for the distribution of each variable using the corresponding values of α_s measured at M_Z. Then all variants of the theory mentioned above are calculated with the same value of α_s. In each bin of the distribution for a given variable, the largest upward and downward differences with respect to the reference theory are taken to define an uncertainty band around the reference theory.

In the last step, the value of α_s in the reference theory is varied, in order to find the range of values which result in predictions lying inside the uncertainty band for the fit range under consideration. The largest and smallest allowed values of α_s fulfilling the condition finally set the perturbative systematic uncertainty. The method is illustrated in Fig. 13, taking the thrust as an example.

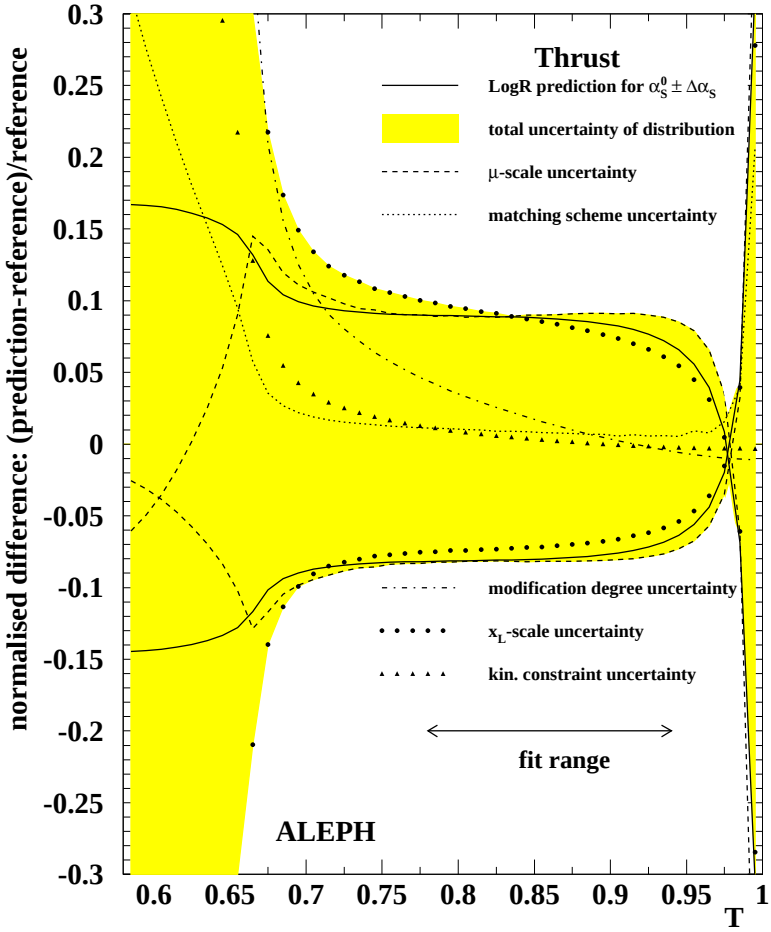

Figure 13: Theoretical uncertainties for the distribution of thrust at LEP1. The grey area represents the perturbative uncertainties of the distribution for a given value α_s^0. Dotted/dashed lines and points show the individual components to the uncertainty. The curves show the reference prediction with $\alpha_s^0 \pm \Delta\alpha_s$. The theoretical uncertainty $\Delta\alpha_s$ is defined as the largest deviation from the nominal α_s^0 still resulting into a prediction lying *inside* the uncertainty band for the actual fit range.

The theoretical error depends on the absolute value of α_s, scaling approximately with α_s^3, and on the fit range. At LEP2 energies the statistical fluctuations are large. In order to avoid biases from downward fluctuations, the theoretical uncertainties are calculated with the value of α_s measured at LEP1. For each variable, the corresponding measurement is evolved to the appropriate energy scale and the uncertainty is calculated for the fit range used at that energy point.

An additional error is evaluated for the b-quark mass correction procedure. This correction has only been calculated to $\mathcal{O}(\alpha_s^2)$; no resummed expressions are yet available.

The difference in α_s obtained with and without mass corrections is taken as systematic error. The total perturbative uncertainty quoted in the tables is the quadratic sum of the errors for missing higher orders and for the mass correction procedure.

The hadronisation model uncertainty is estimated by comparing HERWIG and ARIADNE to PYTHIA for both hadronisation and detector corrections. The maximum change with respect to the nominal result using PYTHIA is taken as systematic error. At LEP2 energies the hadronisation model uncertainty is again subject to statistical fluctuations. These fluctuations are observed from one energy to the next and originate from limited statistics of the fully simulated detector-correction functions. Since non-perturbative effects are expected to decrease with $1/Q$, the energy evolution of hadronisation errors has been fitted to a simple $A + B/Q$ parametrisation. The fit was performed for each variable separately. In the fit procedure a weight scaling with luminosity is assigned to the hadronisation uncertainty at each energy point. This ensures that the hadronisation uncertainty at M_{Z}, which is basically free of statistical fluctuations, is not altered by the procedure.

The perturbative component of the error, which is the dominant source of uncertainty in most cases, is highly correlated between the energy points. The perturbative errors decrease with increasing Q, and faster than the coupling constant itself. The overall error is in general dominated by the combination of renormalisation scale and logarithmic variable rescaling uncertainties.

8 Combined Results

The measurements obtained with the six different variables are combined into a single measurement per energy using weighted averages. A weight is assigned to each observable-dependent measurement α_s^i proportional to the inverse square of its total error $w_i \propto 1/\sigma_i^2$. The weighted average $\overline{\alpha}_s$ is then given by

$$\overline{\alpha}_s = \sum_{i=1}^{N=6} w_i \alpha_s^i \ ,$$

and the combined statistical error is

$$\sigma_{\overline{\alpha}_s}^{\mathrm{stat}} = \sqrt{\sum_{i \neq j}^{N=6} (\sigma_i w_i)^2 + 2\rho_{ij}\sigma_i w_i \sigma_j w_j} \ ,$$

for which the correlation coefficients ρ_{ij} are needed. This correlation between fits of α_s to different variables is obtained using a large number of simulated data samples and turns out to be typically 60%–80%. The correlation of systematic errors is taken into account by recomputing the weighted average for all variations of the analysis, and the change in α_s with respect to the nominal value is taken as error.

The combination of experimental systematic uncertainties at LEP2 energies is obtained using a luminosity-weighted average of the uncertainties between 133 GeV and 206 GeV. Combined results are given in Table 7 and shown in Fig. 14, together with a fit of the QCD expectation. The curve is seen to be in good agreement with the measurements. In

Table 7: Combined results for $\alpha_s(Q)$ as obtained with weighted averages. The last row gives the RMS of results from different variables as a cross check of the perturbative uncertainties.

Q [GeV]	91.2	133	161	172	183	189	200	206
$\alpha_s(Q)$	0.1201	0.1161	0.1175	0.1088	0.1090	0.1101	0.1081	0.1054
stat. error	0.0001	0.0025	0.0037	0.0046	0.0022	0.0015	0.0016	0.0016
exp. error	0.0008	0.0010	0.0010	0.0010	0.0010	0.0010	0.0010	0.0010
pert. error	0.0050	0.0045	0.0044	0.0043	0.0039	0.0038	0.0037	0.0037
hadr. error	0.0016	0.0011	0.0009	0.0009	0.0008	0.0008	0.0007	0.0007
total error	0.0053	0.0054	0.0059	0.0064	0.0047	0.0042	0.0042	0.0042
RMS	0.0045	0.0033	0.0042	0.0035	0.0038	0.0041	0.0046	0.0028

the definition of the χ^2 of the fit only the uncorrelated component of the errors is taken into account, which excludes the perturbative error.

The combined measurements between 133 and 206 GeV are evaluated at the scale of the Z boson mass by using the predicted energy evolution of the coupling constant at three-loop level Eq.(A3.3). The measurements evolved to M_{Z} are given in Table 8. They are again combined using a weighted average, with weights proportional to the inverse square of total errors. In contrast to the combination from different variables, here the measurements are statistically uncorrelated. Correlations between systematic uncertainties are taken into account and all variations of the determination of α_s have been performed for the weighted average.

The final ALEPH result, $\alpha_s(M_{\mathrm{Z}}) = 0.1214 \pm 0.0048$, is given in Table 9. Included in Table 9 is the combination of measurements at LEP2 energies without the point at M_{Z}. The total uncertainty of the combined LEP2 measurement is comparable to that including LEP1 because the dominant perturbative uncertainties are reduced at higher energies, even after evolution to M_{Z}. The measurements at LEP1 and LEP2 are in good agreement with each other and with previously published ALEPH measurements of α_s using event shapes [1, 38].

Table 8: Combined results for $\alpha_s(M_{\mathrm{Z}})$ as obtained with weighted averages and evolved from the scale Q to M_{Z}.

Q [GeV]	91.2	133	161	172	183	189	200	206
$\alpha_s(M_{\mathrm{Z}})$	0.1201	0.1229	0.1285	0.1193	0.1207	0.1227	0.1212	0.1183
stat. error	0.0001	0.0028	0.0044	0.0056	0.0027	0.0018	0.0020	0.0020
exp. error	0.0008	0.0012	0.0013	0.0013	0.0013	0.0012	0.0013	0.0012
pert. error	0.0050	0.0048	0.0048	0.0047	0.0044	0.0042	0.0042	0.0042
hadr. error	0.0016	0.0012	0.0011	0.0010	0.0010	0.0009	0.0009	0.0009
total error	0.0053	0.0058	0.0067	0.0075	0.0054	0.0049	0.0049	0.0048

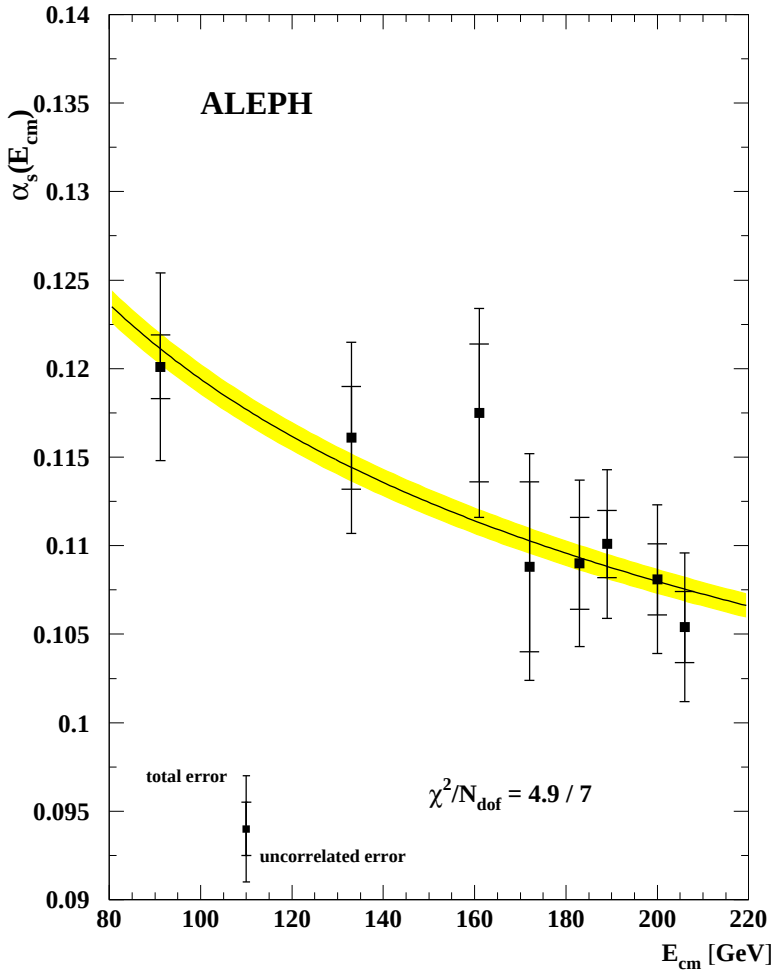

Figure 14: The measurements of the strong coupling constant α_s between 91.2 and 206 GeV. The results using the six different event-shape variables are combined with correlations taken into account. The inner error bars exclude the perturbative uncertainty, which is expected to be highly correlated between the measurements. The outer error bars indicate the total error. A fit of the three-loop evolution formula using the uncorrelated errors is shown. The shaded area corresponds to the uncertainty in the fit parameter of the three-loop formula $\Lambda_{\overline{\mathrm{MS}}} = 247 \pm 14$ MeV, equivalent to $\alpha_s(M_{\mathrm{Z}}) = 0.1211 \pm 0.0008$.

Table 9: Weighted average of combined measurements for $\alpha_s(M_{\mathrm{Z}})$ obtained at energies from 91.2 GeV to 206 GeV and the average without the point at M_{Z}.

data set	LEP1 + LEP2	LEP2
$\alpha_s(M_{\mathrm{Z}})$	0.1214	0.1217
stat. error	$\pm$ 0.0009	$\pm$ 0.0010
exp. error	$\pm$ 0.0011	$\pm$ 0.0012
pert. error	$\pm$ 0.0045	$\pm$ 0.0044
hadr. error	$\pm$ 0.0011	$\pm$ 0.0010
total error	$\pm$ 0.0048	$\pm$ 0.0048

Finally, as a cross check, another combination method is investigated in which a simultaneous fit to data sets at all energies is performed. These simultaneous fits are used in Section 9 to investigate power law corrections. Effectively, this method implies using statistical uncertainties as weights, so that the result is dominated by the precise data at M_Z. This determination of $\alpha_s(M_Z) = 0.1202 \pm 0.0052$ is practically the same as without high energy data.

9 Study of Power Law Corrections

Non-perturbative effects in hadronic observables in e^+e^- annihilation are in general suppressed by powers of $1/Q$ [5]. These effects are small in inclusive quantities such as the total cross section. For most of the event-shape variables, however, the power of the $1/Q$ term is equal to unity, and hadronisation corrections are relatively large (5 - 10 % at $Q = M_Z$). Corrections for hadronisation are usually derived from Monte Carlo generators and applied to perturbative predictions, in order to extract the value of α_s as done in Section 6. Here a comparative study is presented in which α_s is determined both with analytical power corrections and with Monte Carlo corrections. The aim is to test models of power corrections and to evaluate possible improvements for measurements of α_s. Since power corrections scale with $1/Q$, it is important to include data sets from a large range of centre-of-mass energies, which are fit simultaneously for a given variable.

Power corrections in the spirit of [5] are related to infrared divergences of the perturbative expansion at low scales. Analytical calculations introduce one additional phenomenological parameter α_0,

$$\alpha_0(\mu_I) = \frac{1}{\mu_I} \int_0^{\mu_I} \alpha_s(k) dk \ ,$$

which measures effectively the strength of the coupling up to an infrared matching scale μ_I of the order of a few GeV. The parameter α_0 is expected to be universal and must be determined by experiment.

Theoretical predictions exist for mean values and distributions of T, ρ, C, B_W and B_T, and the leading power correction for these variables scales with $1/Q$. No calculations are yet available for y_3 which is expected to receive only a $1/Q^2$ or $\ln Q/Q^2$ correction [5]. Mean values are analysed first, mainly for illustrative purposes; the statistical significance of fits to mean values is inferior to analyses of distributions, and perturbative predictions to second order are used without resummation. The analysis of mean values include measurements at lower energies [39] and of LEP experiments which have employed radiative events [40]. The full systematic study then follows for distributions in a second step using the ALEPH data only. The relevant formulae for power corrections are given in Appendix A4.

9.1 Mean Values

Mean values are subject to a leading power correction proportional to $\alpha_0(\mu_I)/Q$ which is added to the perturbative prediction being itself proportional to $\mathcal{O}(\alpha_s^2)$. The two parameters α_s and α_0 are determined in simultaneous fits to mean value measurements

Table 10: Results of simultaneous fits of α_s and $\alpha_0(2\,\mathrm{GeV})$ using power corrections to mean values of event shapes, including lower energy data. The uncertainties and the correlation between α_s and α_0 are obtained using the fit which includes statistical and systematic uncertainties of the data.

variable	$\alpha_s(M_\mathrm{Z})$	$\alpha_0(2\,\mathrm{GeV})$	χ^2/N_DOF	correlation
T	0.1207 ± 0.0019	0.539 ± 0.011	69/43	−83%
ρ	0.1161 ± 0.0018	0.627 ± 0.020	50/40	−82%
C	0.1228 ± 0.0027	0.461 ± 0.016	17/18	−91%
B_W	0.1179 ± 0.0028	0.467 ± 0.037	11/18	−94%
B_T	0.1148 ± 0.0025	0.492 ± 0.020	7/18	−92%

in the energy range from 12 GeV to 206 GeV. The renormalisation scale x_μ is set to unity and the infrared matching scale μ_I to 2 GeV. Corrections for the b-quark mass are applied for the perturbative prediction in the same way as for the fits using Monte Carlo corrections (see Section 6). The quadratic sum of statistical and experimental systematic errors is included in the definition of the χ^2 of the fit. The fit results are summarised in Table 10 and shown in Fig. 15. For comparison in Table 11 fit results obtained using Monte Carlo corrections are summarised.

The quality of fits with power corrections in terms of χ^2/N_DOF is good and slightly better than for fits with Monte Carlo corrections. The values of α_s between 0.115 and 0.123 are compatible with the combined measurement of α_s given in Section 8. The value of α_0 is around 0.5 except for ρ for which it is 20% larger. The correlation between α_s and α_0 obtained from the fit is large and negative.

It can be seen that the values of α_s with power corrections are systematically lower than with Monte Carlo corrections (Table 11). The large value of α_s with Monte Carlo corrections is not unusual in the framework of fixed order calculations; in general a better description is obtained with an optimised scale $\mu \ll Q$.

Table 11: Results of fits to mean values of event shapes using Monte Carlo corrections. The errors are obtained with the fit which includes statistical and experimental systematic uncertainties.

variable	$\alpha_s(M_\mathrm{Z})$	χ^2/N_DOF
T	0.1285 ± 0.0005	70/44
ρ	0.1273 ± 0.0007	67/41
C	0.1269 ± 0.0006	23/19
B_W	0.1274 ± 0.0007	14/19
B_T	0.1174 ± 0.0005	16/19

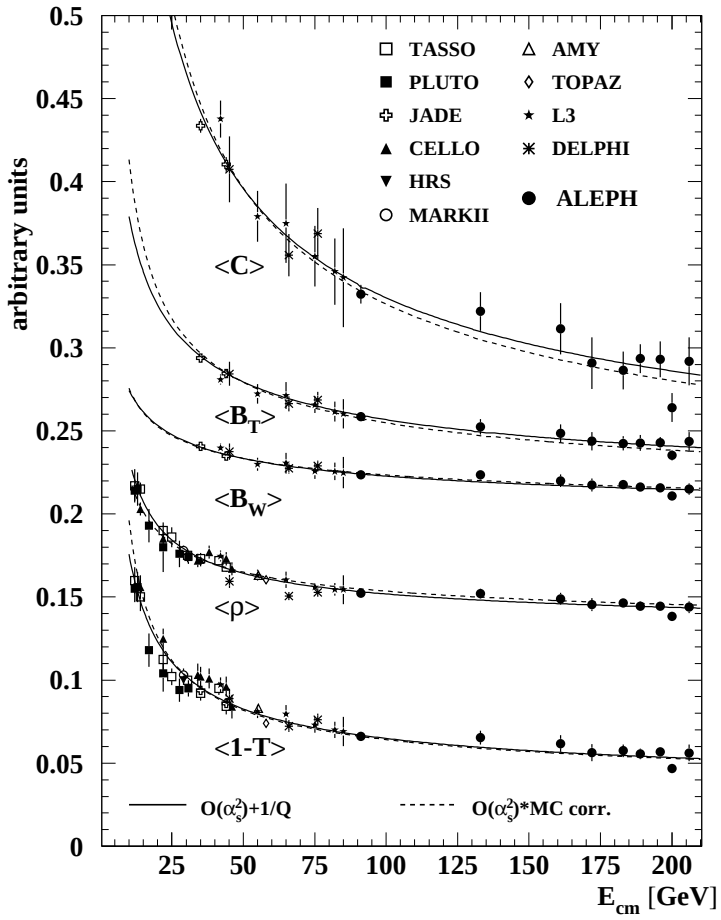

Figure 15: Event-shape mean values (shifted by an arbitrary amount) as function of centre-of-mass energy. The full lines show the result of fits with power corrections, the dashed lines are fits with Monte Carlo correction.

9.2 Distributions

In the simplest model [5] power corrections to distributions are incorporated as a shift of the perturbative prediction by the same amount as the additive correction to mean values. The modified Log(R) matching scheme including corrections for the b-quark mass is used for the perturbative prediction. The shift is constant for T, ρ, and C, but depends on the actual value of the variable for B_W and B_T , leading to a squeeze of the distributions. Simultaneous fits of α_s and α_0 are carried out using only ALEPH data from 91 GeV to 209 GeV within the fit ranges given in Tables 5 and 6. The statistical significance of single data sets at LEP2 is insufficient to determine two parameters simultaneously. Therefore, the distributions of each variable are fit simultaneously at all energies, taking advantage of the $1/Q$ scaling properties of the non-perturbative term. Results with power corrections are given in Table 12; for comparison fits of α_s obtained with Monte Carlo corrections for hadronisation are given in Table 13.

Experimental systematic uncertainties are obtained in the same way for both measurements. The method described in Section 7.2 is extended to two parameters to determine the perturbative uncertainties of α_s and α_0 from the power corrections. In this case the uncertainty bands are evaluated simultaneously at all energies for a given

Table 12: Results of simultaneous fits of α_s and $\alpha_0(2\text{ GeV})$ to distributions at energies between 91 and 206 GeV using power corrections.

Variable	T	ρ	C	B_W	B_T
$\alpha_s(M_Z)$	0.1192	0.1068	0.1159	0.1043	0.1175
stat. error	0.0007	0.0011	0.0007	0.0009	0.0004
exp. error	0.0014	0.0029	0.0015	0.0024	0.0017
pert. error	0.0057	0.0040	0.0059	0.0041	0.0072
non pert. error	0.0001	0.0001	0.0008	0.0001	0.0001
total error	0.0059	0.0051	0.0062	0.0048	0.0074
$\chi^2/N_{\rm DOF}$	73/47	124/42	83/54	76/47	181/59
$\alpha_0(2\text{ GeV})$	0.452	0.808	0.443	0.812	0.667
stat. error	0.012	0.038	0.009	0.047	0.008
exp. error	0.025	0.085	0.035	0.068	0.003
pert. error	0.013	0.024	0.006	0.020	0.009
non pert. error	0.061	0.158	0.043	0.177	0.137
total error	0.068	0.185	0.056	0.196	0.137
correlation	−29%	−45%	−32%	−27%	−25%

variable. Non-perturbative systematic uncertainties for α_s are estimated by varying the infrared matching scale in the range $1\text{ GeV} \leq \mu_{\rm I} \leq 3\text{ GeV}$. Another uncertainty for α_s and α_0 is stemming from missing higher order corrections to the Milan factor (Appendix A4), $\mathcal{M} \to \mathcal{M} \pm \mathcal{O}(\alpha_s/\pi)$. As recommended in [41], $\mathcal{M}$ is varied by ± 0.2 around its nominal value of 1.49.

The quality of the fits with power corrections is again slightly better than with Monte Carlo corrections. The values of α_s are clearly lower than with Monte Carlo corrections, in particular for wide jet broadening and heavy jet mass, on average by 10%. A large spread between the results from different variables is observed. The values of α_0 are grouped in

Table 13: Results of simultaneous fits of α_s to distributions at energies between 91 and 206 GeV using Monte Carlo corrections.

Variable	T	ρ	C	B_W	B_T
$\alpha_s(M_Z)$	0.1264	0.1187	0.1225	0.1164	0.1260
stat. error	0.0001	0.0002	0.0001	0.0002	0.0001
exp. error	0.0008	0.0010	0.0007	0.0006	0.0006
pert. error	0.0063	0.0038	0.0058	0.0051	0.0080
hadr. error	0.0019	0.0014	0.0015	0.0015	0.0029
total error	0.0067	0.0041	0.0061	0.0054	0.0085
$\chi^2/N_{\rm DOF}$	75/48	144/43	88/55	111/48	222/60

three classes of observables: T and C yield 0.45, ρ and B_W give 0.81 and B_T is in between these two classes with a value of 0.67. These results are compatible with each other at the level of two standard deviations.

As can be seen from Table 12, perturbative uncertainties are related mainly to α_s and much less to α_0, and vice versa for non-perturbative uncertainties. Therefore it appears that α_s is mainly determined by the perturbative contribution to the prediction and α_0 is fixed by the power correction part. The perturbative uncertainties for α_s with power corrections are similar to the uncertainties obtained with Monte Carlo corrections. The non-perturbative uncertainties are much smaller than corresponding hadronisation corrections.

The uncertainties of α_0 are between 15% and 25%, and are dominated by the non-perturbative contribution stemming from the uncertainty of the Milan factor. This uncertainty is three times larger for ρ and B_W than for T and C.

The measurements of α_s and α_0 are not independent, the statistical correlation from the fit being typically -95%. The total correlation is modified by systematic effects, and the correlation coefficients are obtained by constructing a total covariance matrix which includes experimental and theoretical uncertainties. The correlation coefficient for experimental systematic effects is also large and negative, typically -60%, but the correlation of theoretical uncertainties is weak and about -10% to -30%.

In Fig. 16 the results of measurements of $\alpha_s(M_Z)$ and α_0 using power corrections are compared to the average value of α_s obtained with the standard method based on Monte Carlo corrections in Table 9. The measurements of α_s and α_0 from the different variables are combined using weighted averages as outlined in Section 8. The total correlation between the weighted averages of α_s and α_0 is obtained using the total covariance matrix of the combined measurement. The results are given in Table 14. These results of α_s and α_0 are consistent with other recent analyses of power law corrections [40, 44]. The value of α_s is found to be significantly lower than that obtained with Monte Carlo corrections (Table 13) and the values of α_0 are universal only within about two standard deviations. A large spread is observed between results using different variables. The determination of α_0 using B_W, ρ and to a lesser extent B_T is affected by large non-perturbative uncertainties, which indicate that missing higher order corrections to the Milan factor may significantly change the value of α_0. Therefore, the numbers of α_s given in this section are not

Table 14: Combined results of simultaneous fits of α_s and α_0(2 GeV) using weighted averages.

parameter	$\alpha_s(M_Z)$	α_0(2 GeV)
central result	0.1112	0.496
stat. error	0.0006	0.006
exp. error	0.0014	0.026
pert. error	0.0050	0.069
non pert. error	0.0001	0.068
total error	0.0053	0.101
correlation	-48%	

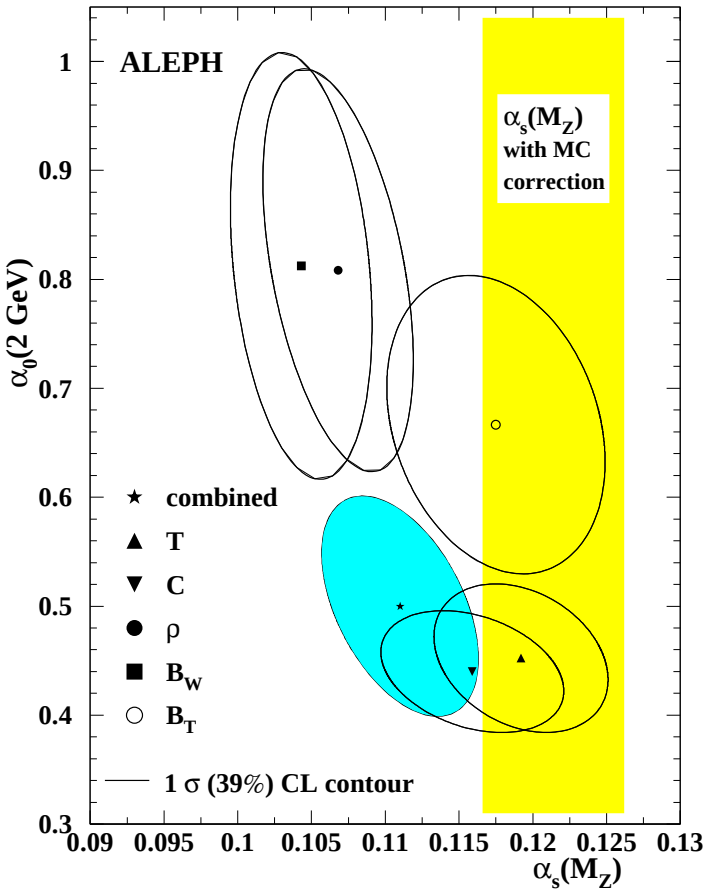

Figure 16: Contours of confidence level for simultaneous measurements of α_s and α_0 (ellipses) compared to the combined measurement of α_s using Monte Carlo corrections (shaded band).

considered as a measurement, but as a test, of power corrections. The discrepancy between α_s using Monte Carlo corrections and $1/Q$ corrections and the universality of α_0 needs to be investigated further.

10 Conclusions

New results have been presented for observables determined from hadronic final states in the data recorded by ALEPH at centre-of-mass energies between 91.2 GeV and 209 GeV. The variables have been treated in a consistent way at all energies.

Inclusive charged particle spectra have been found to be in good agreement with predictions from QCD generators, as is shown in Figs. 1 and 2, except for $p_\perp^{\rm out}$. The energy evolution of the mean charged particle multiplicity and the peak position of the scaled momentum spectrum are illustrated in Figs. 3 and 5 and have been observed to be consistent with MLLA predictions. The evolution of x_E distributions has been compared to global parametrisations of fragmentation functions in Fig. 6.

Measurements of jet rates and various event-shape variables have been carried out and are shown in Figs. 7, 8 and 9. The distributions of thrust, C-parameter, heavy jet mass,

$-\ln y_3$, wide and total jet broadening have been compared to calculations of perturbative QCD in Figs. 10 and 11, and the strong coupling constant has been measured at all energies. The results shown in Fig. 14 have been found to be in good agreement with the expected energy evolution of the running coupling constant. The final combined result is

$$\alpha_s(M_{\mathrm{Z}}) = 0.1214 \pm 0.0048.$$

The precision of the measurement is limited by perturbative uncertainties, which have been scrutinised with a new method.

A model of non-perturbative $1/Q$ power corrections has been investigated and the associated parameter has been determined to be $\alpha_0(2\mathrm{GeV}) = 0.496 \pm 0.101$. The value of α_s determined simultaneously is significantly lower than the nominal result obtained with Monte Carlo hadronisation corrections. For α_0 a large spread of results between different variables, as depicted in Fig. 16, and important non-perturbative uncertainties for wide jet broadening and heavy jet mass have been observed and need to be further investigated.

Acknowledgements

We wish to thank our colleagues from the accelerator divisions for the successful operation of LEP. It is also a pleasure to thank the engineers and technicians of the collaborating institutions for their support in constructing and maintaining the ALEPH experiment. Those of us from non-member states thank CERN for its hospitality.

References

[1] The ALEPH Collaboration, "*Studies of Quantum Chromodynamics with the ALEPH Detector*", Physics Reports **294** (1998) 1.

[2] The ALEPH Collaboration, "*Studies of QCD in $e^+e^- \to$ Hadrons at E_{cm} = 130 and 136 GeV*", Z. Phys. **C 73** (1997) 409.

[3] The ALEPH QCD web site,
`http://alephwww.cern.ch/QCD/evsh.html`

[4] R. Jones, M. Ford, G.P. Salam, H. Stenzel and D. Wicke "*Theoretical uncertainties on α_s from event-shape variables in e^+e^- annihilations*", hep-ph/0312016 (2003)

[5] B.R. Webber, "*Estimation of Power Corrections to Hadronic Event Shapes*", Phys. Lett. **B 339** (1994) 148;
Yu.L. Dokshitzer and B.R. Webber, "*Calculation of Power Corrections to Hadronic Event Shapes*", Phys. Lett. **B 352** (1995) 451;
Yu.L. Dokshitzer, G. Marchesini and B.R. Webber, "*Dispersive Approach to power behaved contributions in QCD hard processes*" , Nucl. Phys. **B 469** (1996) 93;
Yu.L. Dokshitzer and B.R. Webber, "*Power Corrections to Event-Shape Distributions*", Phys. Lett. **B 404** (1997) 321.

[6] The ALEPH Collaboration, "*ALEPH: a detector for electron-positron annihilations at LEP*", Nucl. Instrum. and Methods **A 294** (1990) 121.

[7] The ALEPH Collaboration, "*Performance of the ALEPH Detector at LEP*", Nucl. Instrum. and Methods **A 379** (1995) 101.

[8] S. Catani et al., Phys. Lett. **B 269** (1991) 432;
W.J. Stirling et al., Proceedings of the Durham Workshop, J. Phys. G: Nucl. Part. Phys. **17** (1991) 1567;
N. Brown and W.J. Stirling, Phys. Lett. **B 252** (1990) 657;
S. Bethke et al., Nucl. Phys. **B 370** (1992) 310.

[9] S. Jadach, B.F.L. Ward and Z. Was, "*The Monte Carlo program KORALZ, version 4.0, for the lepton or quark pair production at LEP/SLC energies*", Comput. Phys. Commun. **79** (1994) 503;
Comput. Phys. Commun. **124** (2000) 233.

[10] S. Jadach et al.,, "*Monte Carlo Program KoralW 1.42 for All Four-Fermion Final States in e^+e^- Collisions*", Comput. Phys. Commun. **135** (2001) 238. Comput. Phys. Commun. **119** (1999) no.2-3,272;
Comput. Phys. Commun. **94** (1996) 216.

[11] T. Sjöstrand et al., "*High-Energy-Physics Event Generation with PYTHIA 6.1*", Comput. Phys. Commun. **135** (2001) 238.

[12] G. Corcella et al., "*HERWIG 6: an event generator for Hadron Emission Reactions With Interfering Gluons*", JHEP **0101** (2001) 010.

[13] L. Lönnblad, "*ARIADNE version 4 - A Program for Simulation of QCD Cascades Implementing The Colour Dipole Model* ", Comput. Phys. Commun. **71** (1992).

[14] HEPDATA, The Durham HEP Database, `http://durpdg.dur.ac.uk/HEPDATA/`

[15] The JADE Collaboration, "*Experimental Studies on Multi-Jet Production in e^+e^- at PETRA Energies*", Z. Phys. **C 33** (1986) 23;
The TASSO Collaboration, "*Experimental Study of Jet Masses in e^+e^- Annihilation at C.M. Energies between 12 and 43.5 GeV* ", Z. Phys. **C 22** (1989) 193;
The AMY Collaboration, "*Charged Hadron Multiplicities in e^+e^- Annihilations at $\sqrt{s}$ = 50 GeV - 61.4 GeV*, Phys. Rev. **D 42** (1990) 737;
The HRS Collaboration, "*Study of Quark Fragmentation in e^+e^- Annihilation at 29 GeV*, Phys. Rev. **D 34** (1986) 3304;
The TPC/2γ Collaboration, "*Pion and Kaon Multiplicities in heavy Quark Jets from e^+e^- Annihilation at 29 GeV*, Phys. Lett. **B 184** (1987) 299;
The MARK-II Collaboration, "*Charged Multiplicity of hadronic Events containing heavy Quark Jets*, Phys. Rev. Lett. **54** (1985) 2580;
The TOPAZ Collaboration, "*Charged Particle Multiplicities of Quark and Gluon Jets in e^+e^- Annihilation at TRISTAN*, Phys. Lett. **B 413** (1997) 447.

[16] V.A. Khoze and W. Ochs, "*Perturbative QCD Approach to Multiparticle Production*", Int. J. Mod. Phys. **A 12** (1997) 2949;
Yu.L. Dokshitzer, V.A. Khoze, A.H. Mueller and S.I. Troyan, "*Basics of Perturbative QCD* ", Editions Frontières, Gif-sur-Yvette (1992).

[17] I.M. Dremlin and J.W. Gary, " *Hadron Multiplicities* ", Physics Reports **349** (2001) 301.

[18] C.P. Fong and B.R. Webber, "*Higher-Order QCD Corrections to Hadron Energy Distributions in Jets*" Phys. Lett. **B 229** (1989) 289;
ibid, "*One- and two-particle distributions at small x in QCD Jets*", Nucl. Phys **B 355** (1991) 54.

[19] The TASSO Collaboration, "*Global Jet Properties at 14 GeV to 44 GeV Center-of-Mass Energy in e^+e^- annihilation* ", Z. Phys. **C 47** (1990) 187.

[20] V.N. Gribov and L.N. Lipatov, Sov. J. Nucl. Phys. **15** (1972) 78;
G. Altarelli and G. Parisi, Nucl. Phys. **B126** (1977) 298;
Yu.L. Dokshitzer, Sov. Phys. JETP **46** (1977) 641.

[21] The ALEPH Collaboration, "*Measurement of α_s from Scaling Violations in Fragmentation Functions in e^+e^- Annihilation*", Phys. Lett. **B 357** (1995) 487.

[22] B.A. Kniehl, G. Kramer and B. Pötter, "*Fragmentation Functions for Pions, Kaons and Protons at Next-to-leading Order*", Nucl. Phys. **B 582** (2000) 514.

[23] L. Bourhis, M. Fontannaz, J.P. Guillet and B. Werlen, "*Next-to-leading order determination of fragmentation functions*", Eur. Phys. J. **C19** (2001) 89.

[24] S. Kretzer, "*Fragmentation functions from flavour-inclusive and flavour-tagged e^+e^- annihilations*", Phys. Rev. **D 62** (2000) 054001.

[25] S. Brandt et al., Phys. Lett. **12** (1964) 57;
E. Farhi, Phys. Rev. Lett. **39** (1977) 1587.

[26] T. Chandramohan and L. Clavelli, Nucl. Phys. **B 184** (1981) 365;
L. Clavelli and D. Wyler, Phys. Lett. **B 103** (1981) 383.

[27] P.E.L. Rakow and B.R. Webber, Nucl. Phys. **B 191** (1981) 63.

[28] G. Parisi, Phys. Lett. **B 74** (1978) 65;
J.F. Donoghue, F.E. Low, and S.Y. Pi, Phys. Rev. **D 20** (1979) 2759.

[29] R.K. Ellis, D.A. Ross and A.E. Terrano, Nucl. Phys. **B 178** (1981) 421.

[30] S. Catani et al., "*Resummation of large logarithms in e^+e^- event-shape distributions*", Nucl. Phys. **B 407** (1993) 3;
ibid, "*Thrust distribution in e^+e^- annihilation*", Phys. Lett. **B 269** (1991) 432;
S. Catani, G. Turnock and B.R. Webber, "*Heavy Jet Mass distribution in e^+e^- annihilation*", Phys. Lett. **B 272** (1991) 368.

[31] G. Dissertori and M. Schmelling, "*An improved theoretical prediction for the two jet rate in e^+e^- annihilation*", Phys. Lett. **B 361** (1995) 167.

[32] S. Catani G. Turnock and B.R. Webber, "*Jet broadening measures in e^+e^- annihilation*", Phys. Lett. **B 295** (1992) 269;
Yu.L. Dokshitzer, "*On the QCD analysis of Jet Broadening*", JHEP **9801** (1998) 011.

[33] S. Catani and B.R. Webber, "*Resummed C-parameter distribution in e^+e^- annihilation*", Phys. Lett. **B427** (1998) 377.

[34] A. Banfi, G.P. Salam and G. Zanderighi, "*Semi-numerical resummation of event shapes*", JHEP **0201** (2002) 018.

[35] The ALEPH Collaboration, "*A Measurement of the b-quark Mass from Hadronic Z Decays*", Eur. Phys. J. **C 18** (2000) 1.

[36] P. Nason and C. Oleari, "*Next-to-leading Order Correction to the Production of Heavy Flavor Jets in e^+e^- Collisions*", Nucl. Phys. **B 521** (1998) 237.

[37] M. Dasgupta and G. P. Salam, "*Resummed event-shape variables in DIS*", JHEP **0208** (2002) 032.

[38] The ALEPH Collaboration, "*A measurement of the QCD colour factors and a limit on the light gluino* ", Z. Phys. **C 76** (1997) 1.

[39] The TASSO Collaboration, "*Global jet properties at 14-44 GeV center of mass energy in e^+e^- annihilation*", Z. Phys. **C 47** (1990) 187;
"*Jet Production and Fragmentation in e^+e^- Annihilation at 14-43 GeV*", Z. Phys. **C 22** (1984) 307;
"*Experimental study of jet masses in e^+e^- annihilation at c.m. energies between 12 and 43.5 GeV*", Z. Phys. **C 45** (1989) 11;
The PLUTO Collaboration, "*Energy Dependence of Jet Measures in e^+e^- Annihilation*", Z. Phys. **C 12** (1982) 297;
P.A. Movilla Fernàndez et al. and the JADE Collaboration, "*A Study of Event Shapes and Determinations of α_s using data of e^+e^- Annihilations at $\sqrt{s}$ = 22 to 44 GeV*", Eur. Phys. J. **C 1** (1998) 461;
O. Biebel et al. and the JADE Collaboration, "*C-Parameter and Jet Broadening at PETRA Energies*", Phys. Lett. **B 459** (1999) 326;
The CELLO Collaboration, "*Model-independent limits on $\Lambda_{\rm QCD}$ from e^+e^- annihilation in the energy range from 14 to 46 GeV*", Z. Phys. **C 44** (1989) 63;
The HRS Collaboration, "*Study of quark fragmentation in e^+e^- annihilation at 29 GeV: Global jet parameters and single-particle distributions*", Phys. Rev. **D 31** (1985) 1;
The MARK II Collaboration, "*Multihadronic events at $E_{\rm c.m.}$= 29 GeV and predictions of QCD models from $E_{\rm c.m.}$= 29 GeV to $E_{\rm c.m.}$= 93 GeV*", Phys. Rev. **D 37** (1988) 1;
The AMY Collaboration, "*Multihadron-event properties in e^+e^- annihilation at $\sqrt{s}$ =52-57 GeV*", Phys. Rev. **D 41** (1990) 2675;

The TOPAZ Collaboration, "*Experimental study of b-quark jets in e^+e^- annihilation at TRISTAN*", Phys. Lett. **B 278** (1992) 506.

[40] The DELPHI Collaboration, "*A study of the energy evolution of event shape distributions and their means with the DELPHI detector at LEP*", Eur. Phys. J. **C 29** (2003) 285;
The L3 Collaboration, "*QCD Studies in e^+e^- Annihilation from 30 GeV to 189 GeV*", Phys. Lett. **B 489** (2000) 65.

[41] Yu.L. Dokshitzer et al., "*On the universality of the Milan factor for $1/Q$ power corrections to jet shapes*", JHEP **9805** (1998) 003.

[42] Yu.L. Dokshitzer, "*Perturbative QCD and Power Corrections*", hep-ph/9911299 (1999)

[43] Yu.L. Dokshitzer, G. Marchesini and G.P. Salam, "*Revisiting non-perturbative effects in the jet broadenings*", Eur. Phys. J. direct **C 1** (1999) 3.

[44] P.A. Movilla Fernàndez et al., "*Tests of Power Corrections for Event Shapes in e^+e^- Annihilation*", Eur. Phys. J. **C 22** (2001) 1;
The H1 Collaboration, "*Investigation of Power Corrections to Event Shape Variables measured in Deep-Inelastic Scattering*", Eur. Phys. J. **C 14** (2000) 255, Erratum ibid **C 18** (2000) 417.

A Theoretical Predictions

A1 Mean charged particle multiplicity

The asymptotic prediction for $\langle N_{\rm ch}\rangle$ at large Y is given by [16]

$$\ln\langle N_{\rm ch}\rangle = K_{\rm LPHD}\,\frac{8}{9}\,\exp\left(\sqrt{\frac{32\pi N_c}{\alpha_s(Y)}}\,\frac{1}{b} + \left[\frac{B}{2}-\frac{1}{4}\right]\ln\alpha_s(Y)\right)\ , \tag{A1.1}$$

where

$$Y = \ln Q/2\Lambda\ ,\quad B = \frac{a}{b}\ ,\quad a = \frac{11}{3}N_c + \frac{2n_f}{3N_c^2}\ ,\quad b = \frac{11}{3}N_c - \frac{2}{3}n_f\ ,$$

with the number of colours N_c and the number of flavours n_f. The mean multiplicity corresponding to the limiting spectrum reads as [16]

$$\langle N_{\rm ch}\rangle = K_{\rm LPHD}\,\frac{8}{9}\,\Gamma(B)\left(\frac{z}{2}\right)^{-B+1}\ I_{B+1}(z)\ , \tag{A1.2}$$

where $z = \sqrt{\frac{16N_c}{b}Y}$ and I_B is the modified Bessel function of order B. Higher order corrections to the MLLA prediction of Eq.(A1.2) have been calculated in [17], resulting

in the expression

$$\begin{aligned}\langle N_{\rm ch}\rangle &= \frac{K_{\rm LPHD}}{r_0}\, Y^{-a_1c^2}\, \exp\left(2c\sqrt{Y}+\frac{c}{\sqrt{Y}}\left[r_1+2a_2c^2+\frac{\beta_1}{\beta_0^2}(\ln 2Y+2)\right]\right.\\ &\left.+\frac{c^2}{Y}\left[a_3c^2+\frac{r_1^2}{2}+r_2-\frac{a_1\beta_1}{\beta_0^2}(\ln 2Y+1)\right]\right)\ , \qquad \text{(A1.3)}\end{aligned}$$

where

$$c=\left(\frac{4N_c}{\beta_0}\right)^{1/2}\ ,\ \ \beta_0=\frac{11N_c-2n_f}{3}\ ,\ \ \beta_1=\frac{17N_c^2-n_f(5N_c+3C_F)}{3}\ ,\ \ C_F=\frac{4}{3}\ ,$$

and the coefficients a_i and c_i depend on n_f. Their numerical values can be found in [17].

A2 Inclusive scaled momentum spectrum and peak position

The distribution of $\xi=-\ln x_p$ in the MLLA approximation of the limiting spectrum is given by [16]

$$\begin{aligned}\frac{1}{\sigma}\frac{d\sigma}{d\xi} &= 2\,\frac{C_F}{N_c}\,K_{\rm LPHD}\,\frac{4N_c}{b}\,\Gamma(B)\int_{-\frac{\pi}{2}}^{\frac{\pi}{2}}\frac{dz}{\pi}\,e^{-B\alpha}\left[\frac{\cosh\alpha+(1-2t)\sinh\alpha}{\frac{4N_c}{b}\,Y\,\frac{\alpha}{\sinh\alpha}}\right]^{\frac{B}{2}}\\ &\times\, I_B\left(\sqrt{\frac{16N_c}{b}\,Y\,\frac{\alpha}{\sinh\alpha}\,[\cosh\alpha+(1-2t)\sinh\alpha]}\right)\ , \qquad \text{(A2.1)}\end{aligned}$$

with

$$\alpha=\alpha_0+iz\ \ ,\ t=1-\frac{\xi}{Y}\ \ ,\ \alpha_0=\operatorname{arctanh}(2t-1)\ .$$

The limiting spectrum determines both the shape and the normalisation as function of Λ and the global hadronisation constant $K_{\rm LPHD}$. The prediction of the distorted Gaussian is defined as [18]

$$\frac{1}{\sigma}\frac{d\sigma}{d\xi}=\frac{N_{\rm ch}}{\sigma\sqrt{2\pi}}\exp\left(\frac{1}{8}k-\frac{1}{2}s\delta-\frac{1}{4}(2+k)\delta^2+\frac{1}{6}s\delta^3+\frac{1}{24}k\delta^4\right)\ , \qquad \text{(A2.2)}$$

where $\delta=(\xi-\overline{\xi})/\sigma$ with the mean value $\overline{\xi}$, the width σ, the skewness s and the kurtosis k. The shape parameters are given by

$$\begin{aligned}\overline{\xi} &= \frac{Y}{2}\left(1+\frac{\rho}{24}\sqrt{\frac{48}{\beta_0Y}}\right)+\overline{\xi}_{\mathcal{O}(1)}\ ,\\ \sigma &= \sqrt{\frac{Y}{3}}\left(\frac{\beta_0Y}{48}\right)^{\frac{1}{4}}\left(1-\frac{\beta_0}{64}\sqrt{\frac{48}{\beta_0Y}}\right)\ ,\\ s &= -\frac{\rho}{16}\sqrt{\frac{3}{Y}}\left(\frac{48}{\beta_0Y}\right)^{\frac{1}{4}}\ ,\\ k &= -\frac{27}{5Y}\left(\sqrt{\frac{\beta_0Y}{48}}-\frac{\beta_0}{48}\right)\ , \qquad \text{(A2.3)}\end{aligned}$$

where $\rho = 11 + 2n_f/N_c^3$ and the correction to the mean $\overline{\xi}_{\mathcal{O}(1)}$ has to be determined experimentally. The energy evolution of ξ^* is given by [16]

$$\xi^* = Y\left(\frac{1}{2} + \sqrt{\frac{c}{Y}} - \frac{c}{Y}\right) , \tag{A2.4}$$

where

$$c = \frac{a^2}{16N_c b} .$$

The formula applies for peak positions determined either with the limiting spectrum or with the distorted Gaussian.

A3 Event-shape distributions

To second order in α_s, the distribution of a generic event-shape variable $y\,(y = 1 - T, \rho, B_W, B_T, y_3, C)$ is given by

$$\frac{1}{\sigma_{\rm tot}}\frac{d\sigma(y)}{dy} = \overline{\alpha}_s(\mu^2)A(y) + \left(\overline{\alpha}_s(\mu^2)\right)^2\left[A(y)2\pi b_0 \ln x_\mu^2 + B(y)\right] , \tag{A3.1}$$

$$\text{where } \overline{\alpha}_s = \frac{\alpha_s}{2\pi} , \; b_0 = \frac{33-2n_f}{12\pi} , \; x_\mu = \frac{\mu}{Q} , \; \mu = \text{renormalisation scale.} \tag{A3.2}$$

The evolution of the running coupling constant at three-loop level is given as function of the scale parameter $\Lambda_{\overline{\rm MS}}$ by

$$\begin{aligned}\alpha_s(\mu) &= \frac{\pi}{\gamma_0 \ln(\mu^2/\Lambda^2)}\left[1 - \frac{\gamma_1}{\gamma_0^2}\frac{\ln\left[\ln(\mu^2/\Lambda^2)\right]}{\ln(\mu^2/\Lambda^2)} + \frac{1}{\gamma_0^2\ln^2(\mu^2/\Lambda^2)}\right.\\ &\quad\left.\times\left(\frac{\gamma_1^2}{\gamma_0^2}\left\{\ln^2(\mu^2/\Lambda^2) - \ln\left[\ln(\mu^2/\Lambda^2)\right] - 1\right\} + \frac{\gamma_2}{\gamma_0}\right)\right] ,\end{aligned} \tag{A3.3}$$

with

$$\gamma_0 = \frac{33-2\,n_f}{12} , \quad \gamma_1 = \frac{153-19\,n_f}{24} , \quad \gamma_2 = \frac{1}{64}\left[\frac{2857}{2} - \frac{5033}{18}\,n_f + \frac{325}{54}\,n_f^2\right] .$$

The coefficient functions A and B are obtained by integrating the ERT [29] matrix elements. The cumulative cross section is defined as

$$R(y,\alpha_s) \equiv \frac{1}{\sigma_{\rm tot}}\int_0^y \frac{d\sigma(x,\alpha_s)}{dx}dx , \tag{A3.4}$$

which may be cast into the second-order form

$$R^{\mathcal{O}(\alpha_s^2)}(y,\alpha_s) = 1 + \mathcal{A}(y)\overline{\alpha}_s + \left[\mathcal{A}(y)2\pi b_0 \ln x_\mu^2 + \mathcal{B}(y)\right]\overline{\alpha}_s{}^2 , \tag{A3.5}$$

where $\mathcal{A}$ and $\mathcal{B}$ are integrated forms of A and B, and the explicit scale dependence for α_s has been dropped.

The prediction of the *Log(R)* matching scheme is given by [30]

$$\begin{aligned} \ln R(y,\alpha_s) &= Lg_1(\alpha_s L) + g_2(\alpha_s L) - (G_{11}L + G_{12}L^2)\overline{\alpha}_s \\ &- (G_{22}L^2 + G_{23}L^3)\overline{\alpha}_s{}^2 + \mathcal{A}(y)\overline{\alpha}_s + \left[\mathcal{B}(y) - \frac{1}{2}\mathcal{A}^2(y)\right]\overline{\alpha}_s{}^2 \,, \end{aligned} \tag{A3.6}$$

with $L = \ln(y_0/y)$ where $y_0 = 1$ for $y = 1-T, \rho, y_3, B_T, B_W$ and $y_0 = 6$ for C. Expressions for the functions g_1 and g_2, which resum leading and next-to-leading logarithms to all orders in α_s, can be found in the literature [30]-[34]. A recent evaluation of the matching coefficients G_{ij} is given in [4]. A kinematic constraint is imposed to the modified Log(R) matching scheme to guarantee that the prediction of the distribution vanishes at a given value $y_{\max}$,

$$\ln R(y_{\max}) = 0 \,, \quad \frac{1}{\sigma_{\rm tot}} \frac{d\sigma(y)}{dy}\bigg|_{y=y_{\max}} = \frac{dR}{dy}\bigg|_{y=y_{\max}} = 0 \,. \tag{A3.7}$$

To fulfil this constraint L is replaced by

$$\tilde{L} = \frac{1}{p}\ln\left(\left(\frac{y_0}{y}\right)^p - \left(\frac{y_0}{y_{\max}}\right)^p + 1\right) \,. \tag{A3.8}$$

The power p is usually chosen equal to unity, the case $p = 2$ is called second degree modification. The values of $y_{\max}$ for the variables used here are taken from [4]. Hence the prediction of the *modified Log(R)* matching scheme is simply obtained by replacing L by $\tilde{L}$ in Eq.(A3.6).

The expression for the R matching scheme reads as [30]

$$\begin{aligned} R(y,\alpha_s) &= (1 + C_1\overline{\alpha}_s + C_2\overline{\alpha}_s{}^2)\exp\left[Lg_1(\alpha_s L) + g_2(\alpha_s L) + G_{21}L\overline{\alpha}_s{}^2\right] \\ &- G_{21}L\overline{\alpha}_s{}^2 - \left[C_1 + G_{11}L + G_{12}L^2\right]\overline{\alpha}_s \\ &- \left[C_2 + C_1(G_{11}L + G_{12}L^2) + \frac{1}{2}(G_{11}L + G_{12}L^2)^2 + (G_{22}L^2 + G_{23}L^3)\right]\overline{\alpha}_s{}^2 \\ &+ \mathcal{A}(y)\overline{\alpha}_s + \mathcal{B}(y)\overline{\alpha}_s{}^2 \,. \end{aligned} \tag{A3.9}$$

The constraints for the modified R matching are the same as for Log(R), Eq.(A3.7). Here a simple modification of L does not satisfy the second constraint. Therefore, L is modified and the matching coefficients G_{11} and G_{21} become functions of y according to the condition

$$\tilde{L}(y_{\max}) = 0 \,, \; \tilde{G}_{11}(y_{\max}) = 0 \,, \; \tilde{G}_{21}(y_{\max}) = 0 \,. \tag{A3.10}$$

This is achieved with the following modification

$$\begin{aligned} \tilde{L}(y) &= \frac{1}{p}\ln\left[\left(\frac{y_0}{y}\right)^p - \left(\frac{y_0}{y_{\max}}\right)^p + 1\right] \,, \\ \tilde{G}_{11}(y) &= G_{11}\left[1 - \left(\frac{y}{y_{\max}}\right)^p\right] \,, \\ \tilde{G}_{21}(y) &= G_{21}\left[1 - \left(\frac{y}{y_{\max}}\right)^p\right] \,. \end{aligned} \tag{A3.11}$$

Finally, the expression for the *modified* R matching scheme can be written as

$$\begin{aligned}
\tilde{R}(y,\alpha_s) &= (1+C_1\overline{\alpha}_s+C_2\overline{\alpha}_s{}^2)\exp\left[\tilde{L}g_1(\alpha_s\tilde{L})+g_2(\alpha_s\tilde{L})-\left(\frac{y}{y_{\max}}\right)^p G_{11}\overline{\alpha}_s\tilde{L}+\tilde{G}_{21}\tilde{L}\overline{\alpha}_s{}^2\right] \\
&- \tilde{G}_{21}\tilde{L}\overline{\alpha}_s{}^2-\left[C_1+\tilde{G}_{11}\tilde{L}+G_{12}\tilde{L}^2\right]\overline{\alpha}_s \qquad \text{(A3.12)} \\
&- \left[C_2+C_1(\tilde{G}_{11}\tilde{L}+G_{12}\tilde{L}^2)+\frac{1}{2}(\tilde{G}_{11}\tilde{L}+G_{12}\tilde{L}^2)^2+(G_{22}\tilde{L}^2+G_{23}\tilde{L}^3)\right]\overline{\alpha}_s{}^2 \\
&+ \mathcal{A}(y)\overline{\alpha}_s+\mathcal{B}(y)\overline{\alpha}_s{}^2 \,.
\end{aligned}$$

The renormalisation scale dependence enters in the coupling constant $\alpha_s(\mu)$ and in the second order terms of the predictions. Explicitly, for $x_\mu \neq 1$, the following terms acquire a scale dependence,

$$\begin{aligned}
\mathcal{B}(y) &\to \overline{\mathcal{B}}(y)=\mathcal{B}(y)+2\pi b_0\,\mathcal{A}(y)\ln x_\mu^2\,, \qquad \text{(A3.13)} \\
G_{21} &\to \overline{G}_{21}=G_{21}+2\pi b_0\,G_{11}\ln x_\mu^2\,, \\
G_{22} &\to \overline{G}_{22}=G_{22}+2\pi b_0\,G_{12}\ln x_\mu^2\,, \\
C_2 &\to \overline{C}_2=C_2+2\pi b_0\,C_1\ln x_\mu^2\,, \\
g_2(\alpha_s L) &\to \overline{g}_2(\alpha_s L)=g_2(\alpha_s L)+b_0\,(\alpha_s L)^2\;g_1'(\alpha_s L)\ln x_\mu^2\,,
\end{aligned}$$

where $g_1'(x)$ refers to the derivative with respect to x. The resummation in terms of the logarithmic variable $L=\ln\frac{y_0}{y}$ can be re-written in terms of a rescaled variable $\widehat{L}=\ln\frac{y_0}{y\cdot x_L}$. Such a rescaling alters the resummed formulae for the modified predictions according to

$$\tilde{L} \to \widehat{L}=\frac{1}{p}\ln\left[\left(\frac{y_0}{x_L\cdot y}\right)^p-\left(\frac{y_0}{x_L\cdot y_{\max}}\right)^p+1\right]\,, \qquad \text{(A3.14)}$$

$$g_1(\alpha_s L) \to \widehat{g}_1=g_1(\alpha_s\widehat{L})\,, \qquad \text{(A3.15)}$$

$$g_2(\alpha_s L) \to \widehat{g}_2=g_2(\alpha_s\widehat{L})+\ln x_L\frac{d}{d\widehat{L}}\left(\widehat{L}g_1(\alpha_s\widehat{L})\right)\,. \qquad \text{(A3.16)}$$

Rescaling the logarithmic variable also entails changes to the fixed-order coefficients both in the modified and unmodified cases

$$\begin{aligned}
G_{12} &\to \widehat{G}_{12}=G_{12} \qquad \text{(A3.17)} \\
G_{11} &\to \widehat{G}_{11}=G_{11}+2G_{12}\ln x_L \\
G_{23} &\to \widehat{G}_{23}=G_{23} \\
G_{22} &\to \widehat{G}_{22}=G_{22}+3G_{23}\ln x_L \\
G_{21} &\to \widehat{G}_{21}=G_{21}+2G_{22}\ln x_L+3G_{23}\ln^2 x_L \\
C_1 &\to \widehat{C}_1=C_1+G_{11}\ln x_L+G_{12}\ln^2 x_L \\
C_2 &\to \widehat{C}_2=C_2+(C_1G_{11}+G_{21})\ln x_L+(C_1G_{12}+G_{22}+\tfrac{1}{2}G_{11}^2)\ln^2 x_L \\
&\qquad +(G_{23}+G_{12}G_{11})\ln^3 x_L+\tfrac{1}{2}G_{12}^2\ln^4 x_L.
\end{aligned}$$

For the modified R matching scheme, the modification factors of the type $\left[1-\left(\frac{y}{y_{\max}}\right)^p\right]$ of Eq.(A3.11) are to be applied to $\widehat{G}_{11}$ and $\widehat{G}_{21}$ after the x_L variation.

A4 Power Corrections

A4.1 Mean Values

The theoretical prediction for the mean value $\langle y \rangle$ of an event-shape variable may be cast into the form

$$\langle y \rangle = \langle y \rangle^{\rm pert} + \langle y \rangle^{\rm pow} \ ,$$

where the perturbative part can be written to second order in α_s as

$$\langle y \rangle^{\rm pert} = A_y \overline{\alpha}_s + B_y \overline{\alpha}_s{}^2 \ , \tag{A4.1}$$

with known coefficients A_y and B_y. The power correction term $\langle y \rangle^{\rm pow}$ is given by [41]

$$\langle y \rangle^{\rm pow} = a_y \mathcal{P} \ \text{ with } \ a_T = 2 \ , \ a_\rho = 1 \ , \ a_C = 3\pi \ , \ a_{B_W} = \frac{1}{2} f_{B_W} \ , a_{B_T} = f_{B_T} \ , \tag{A4.2}$$

and

$$\mathcal{P} = \frac{4C_F}{\pi^2} \mathcal{M} \frac{\mu_{\rm I}}{Q} \left[\alpha_0(\mu_{\rm I}) - \alpha_s(Q) - \frac{\beta_0}{2\pi} \left(\ln \frac{Q}{\mu_{\rm I}} + \frac{K}{\beta_0} + 1 \right) \alpha_s^2(Q) \right] \ , \tag{A4.3}$$

where

$$\mathcal{M} = 1 + \frac{1.575 C_A - 0.104 n_f}{\beta_0} \ , \ K = C_A \left(\frac{67}{18} - \frac{\pi^2}{6} \right) - \frac{5}{9} n_f \ , \ C_A = 3 \ .$$

The Milan factor $\mathcal{M}$ includes two-loop corrections and its value is 1.49 for $n_f = 3$ [42]. The power correction term for the wide and total jet broadenings receives an additional skew

$$f_{B_W} = \frac{\pi}{2\sqrt{2C_F \alpha_{\rm CMW}}} + \frac{3}{4} - \frac{\beta_0}{12 C_F} + \eta_0 \ , \tag{A4.4}$$

$$f_{B_T} = \frac{\pi}{2\sqrt{2C_F \alpha_{\rm CMW}}} + \frac{3}{4} - \frac{\beta_0}{6 C_F} + \eta_0 \ , \tag{A4.5}$$

where $\eta_0 = -0.6137056$ and $\alpha_{\rm CMW}$ is to be evaluated at the scale $Q' = Qe^{-3/4}$ according to

$$\alpha_{\rm CMW} = \alpha_s(Q') \left(1 + K \frac{\alpha_s(Q')}{2\pi} \right) \ .$$

A4.2 Distributions

In event-shape distributions the effect of power corrections is to shift the perturbative spectra by the same amount as the correction to mean values

$$\frac{1}{\sigma} \frac{d\sigma(y)}{dy}^{\rm corrected} = \frac{1}{\sigma} \frac{d\sigma(y - \Delta y)}{dy}^{\rm pert} \ , \ \Delta y = a_y \mathcal{P} \ . \tag{A4.6}$$

The concept of a constant shift Δy does not apply not to jet broadenings [43], where the shift is B-dependent ($B = B_W, B_T$) and acts on the cumulative cross section

$$R(B) = \frac{1}{\sigma} \int_0^B \frac{d\sigma}{dB} db = R^{\rm pert} \left(B - a_B \mathcal{P} f_B(B) \right) \ . \tag{A4.7}$$

For the wide jet broadening the B_W-dependent shift reads as follows

$$f_{B_W} = \ln \frac{1}{B_W} + \eta_0 - 2 - \rho(\mathcal{R}') + \chi(\mathcal{R}') + \psi(1+\mathcal{R}') - \psi(1) \tag{A4.8}$$

where $\psi(x)$ is the derivative of the logarithm of $\Gamma(x)$ and

$$\mathcal{R}' = 2C_F \frac{\alpha_s(B_W\, Q)}{\pi} \left(\ln \frac{1}{B_W} - \frac{3}{4} \right) \quad , \tag{A4.9}$$

and

$$\rho(x) = \int_0^1 dz \left(\frac{1+z}{2z\lambda(x)} \right)^{-x} \ln z(1+z) \quad , \quad \chi(x) = \frac{2}{x} \left([\lambda(x)]^x - 1 \right) \tag{A4.10}$$

with

$$[\lambda(x)]^{-x} = \int_0^1 dz \left(\frac{1+z}{2z} \right)^{-x} . \tag{A4.11}$$

For the wide jet broadening the B_T-dependent shift is given by

$$\begin{aligned} f_{B_T} &= f_{B_W}(B_T) + \psi(1+2\mathcal{R}') - \psi(1+\mathcal{R}') + \frac{1}{2} H(\mathcal{B}^{-1}) \, , \\ H(x) &= \int_x^{z_0} \frac{dz}{z} e^{\mathcal{R}(x)-\mathcal{R}(z)} \frac{\Gamma\left[1+2\mathcal{R}'\right]}{\Gamma\left[1+\mathcal{R}'+\mathcal{R}'(z)\right]} \, , \; \mathcal{B} = \frac{2B_T}{e^{\gamma_E}\lambda(\mathcal{R}')} \, , \\ \mathcal{R}(x) &= -\frac{4C_F}{\beta_0} \left[\left(L - \frac{3}{4} \right) \ln \left(1 - \frac{\ln x}{L} \right) + \ln x \right] \, , \end{aligned} \tag{A4.12}$$

where z_0 corresponds to the Landau pole in $\mathcal{R}(z)$ when the integrand vanishes and L is defined as $L = 2\pi/(\beta_0\, \alpha_{\rm CMW}(Q))$. In order to fulfil the kinematic constraint of Eq.(A3.7) for vanishing predictions at $y_{\rm max}$ for the modified matching schemes, the power correction is modified as well according to

$$\Delta y \to \tilde{\Delta} y = a_y \mathcal{P} \left(1 - \frac{y}{y_{\rm max}} \right)^{np} \quad , \tag{A4.13}$$

with np=2 as suggested in [37].